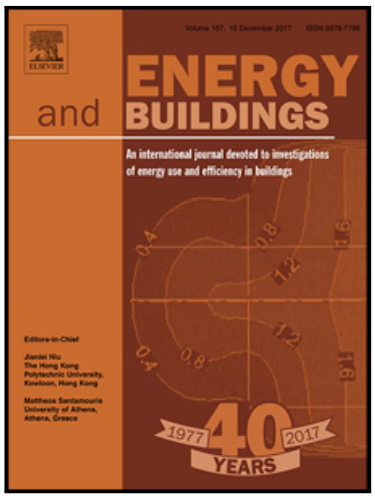

Predicting the thermal behaviour of sands considering its moisture content and grain size with applications to geothermal heat pump installations

Agustín Torres-Rodríguez , David Morillón-Gálvez , Daniel Aldama-Ávalos , José Diego Morales-Ramírez , Iván García Kerdan

PII: S0378-7788(18)33620-X
DOI: https://doi.org/10.1016/j.enbuild.2019.04.005
Reference: ENB 9119

To appear in: *Energy & Buildings*

Received date: 30 November 2018
Revised date: 24 March 2019
Accepted date: 3 April 2019

Please cite this article as: Agustín Torres-Rodríguez , David Morillón-Gálvez , Daniel Aldama-Ávalos , José Diego Morales-Ramírez , Iván García Kerdan , Predicting the thermal behaviour of sands considering its moisture content and grain size with applications to geothermal heat pump installations, *Energy & Buildings* (2019), doi: https://doi.org/10.1016/j.enbuild.2019.04.005

Highlights

- An experimental thermal study of five different types of sands has been conducted
- Fine-grained sands attain higher maximum temperature than coarse-grained sands
- Sub-angular and rounded grains with 0-25% moisture could enhance GHPS performance
- Derivation of a sand temperature model considering grain size, shape and moisture content
- Potential implementation of the derived model in building simulation tools is discussed

Predicting the thermal behaviour of sands considering its moisture content and grain size with applications to geothermal heat pump installations

Agustín Torres-Rodríguez[a], David Morillón-Gálvez[b], Daniel Aldama-Ávalos[c], José Diego Morales-Ramírez[d], Iván García Kerdan[b,e*]

[a]Posgrado de Arquitectura, Universidad Nacional Autónoma de México, 04510 Ciudad de México, México
[b]Instituto de Ingeniería, Universidad Nacional Autónoma de México, 04510 Ciudad de México, México
[c]Facultad de Estudios Superiores Aragón, Universidad Nacional Autónoma de México, 57178 Estado de México, México
[d]Coordinación de Investigación en Arquitectura, Urbanismo y Paisajismo, Universidad Nacional Autónoma de México, 04510 Ciudad de México, México
[e]Department of Chemical Engineering, Imperial College London, London, UK, SW7 2AZ

Abstract

Space conditioning has one of the highest end-use service demands in the building sector. To avoid negative effects on the energy system and the environment, efficient energy sources and technologies must be implemented to provide future heating and cooling requirements. Geothermal heat pump systems (GHPS) are one of the technologies with highest thermodynamic and cost performance; nevertheless, its performance highly depends on local geological characteristics. In this study, a thermodynamic assessment of different types of sands, that could potentially be used as energy sources for GHPS in dry regions, has been conducted. The experiment focuses on understanding the thermal behaviour of five dry sand samples with different standard sieve sizes according to ASTM designations (Nos. 50, 45, 30, 16, and 14) and moisture content capacities. Based on the obtained data, a mathematical model to predict sand temperatures has been derived considering grain size, shape and moisture content. Compared to previous models, our results show that the developed model computed more accurate approximations compared to actual temperatures, providing a robust thermal behaviour model of dry regions' sands that could be used in building simulation tools more effectively.

Keywords: geothermal heat pumps; sand; grain size**;** moisture; mathematical model; temperature.

* Corresponding author. E-mail: i.garcia-kerdan@imperial.ac.uk; IGarciaK@iingen.unam.mx

1. Introduction

One of the main advantages of geothermal heat pump systems (GHPS) is its high energy performance levels. On average, 40-60% less energy is required compared to conventional Heating, Ventilation and Air Conditioning (HVAC) systems and air-source heat pumps (ASHP) (Hakkaki-Fard, Eslami-Nejad et al. 2015). However, the performance of GHPS systems greatly depends on local geological characteristics. GHPS may enhance its performance when a geothermal heat exchanger is buried in thermally enhanced materials. Noorollahi et al. (2018) concluded that an increase in the thermal conductivity of the backfill material can reduce the length of the geothermal heat exchanger (GHE). These installations commonly use a mixture of concrete, clay, lime, cement, and sand with high thermal conductivity as backfill material in the boreholes. Among those geomaterials, sand has been used for filling the boreholes due to lower costs, while maintaining good thermal properties. For instance, Spilker (1998) suggested using sand as backfill material instead of standard bentonite grout to reduce the length of the GHE. Hepbasli, Akdemir et al. (2003) reported that the length of a GHE could be reduced by 15% to 20% when sand is used as heat source instead of bentonite grout. Wood et al. (2010) stated that in soils with high thermal diffusivity, such as wet sand, the heat flux can penetrate much deeper than in drier soils, and this thermal diffusivity depends on the soil thermal conductivity, specific heat capacity and density.

Shang et al. (2014) showed that during the operation of a GHPS installed in Dalian, China, the soil temperature descended more rapidly when using clay as backfill geomaterial compared to sandy clay and sand. The authors concluded that this thermal behavior was due to larger sand's specific heat capacity, thermal conductivity and thermal diffusivity compared to the other backfill materials. Kupiec et al. (2015) observed that when the ambient air temperature is lower than the ground temperature (winter season) the heat is transferred from the lower exchanger (pipes located under the surface of the ground) to the upper exchanger (condenser). Otherwise, the direction of the heat transfer is reversed (if the system is used in the cooling mode). Also, in horizontal geothermal heat exchangers, the shallow layers of the ground are being cooled as a result of the extraction of heat from the ground, as these layers are in a direct contact with the environment. This causes the cold ground to absorb more heat from the environment in winter and lose less heat in summer season. In this regard, apart from the equipment thermal properties,

surface and sub-surface temperatures need to be appropriately determined to optimise the system´s performance and minimise its capital and operational cost.

In dry regions with extreme seasons, sands could be good candidates to be used in sand-air heat exchange processes. For example, an experimental study of a sand–air heat exchanger coupled with a high-temperature solar gas turbine system demonstrated the usefulness of sand as a medium of the heat transfer and energy storage in central receiver systems (Abu-Hamdeh et al. 2001). Abu-Hamdeh et al. (2001) concluded that an increase in moisture content at a given density increases thermal conductivity and at a given moisture content the higher the soil density an increase in thermal conductivity can be observed.

Although sand as a material can be a viable medium for both accumulating and emitting heat, a large variation in its thermal behaviour, both measured and calculated, has been reported in the literature. Nobel and Geller (1987) provided some thermal measurements and models of soils in the California desert. Outputs suggest a simulated and measured temperature of about 22 °C at a depth of 9 cm after 16 hours of solar time. Further simulations of wet soil with 0 % shading yielded a maximum soil temperature of 27 °C. Variability in the results suggest that changes in solar radiation caused by the clouds was the main cause of large differences in soils' temperatures. In a different study, Herb et al. (2008) reported a simulated temperature of 41 °C as an average daily maximum surface temperature in a bare soil in Minnesota, USA. The authors computed a relatively high error in their simulations of bare soil due to inaccuracies in their assumptions on water content and the evaporation process.

Ozgener et al., 2013, studied soil comprised of a mixture of clay, sand and little rocks. The highest measured temperature from the Izmir State Meteorological Center was of around 36 °C to a depth of 20 cm, while the highest soil temperature computed with a theoretical model was of 32 °C (estimated error of 10.26 % between the measurements and model). The high calculated temperatures had lower values than the high temperatures measured and computed in the three stages of the experimental study. In this regard, the authors concluded that dry sand with No. 30 ASTM (American Society for Testing and Materials) attains a higher temperature than wet sand with the same grain size; however, its temperature is lower than the same dry sand contained in a beaker that is covered with round glass. Based on the studied characteristics, a heat sink for a GHPS should consider dry sand with No. 30 ASTM, with large number of black grains with angular shape

contained in large cylindrical container with thermal insulation and covered with round glass. Measurements on these samples were also conducted in other regions in Turkey (Yener et al., 2017). Yener et al. (2017) concluded that the soil temperature greatly depends on parameters such as thermal conductivity, climatic conditions and moisture content.

Jebamalar et al. (2012) observed a maximum temperature of 35 °C in sandy, clay and loam soils in Tatucorin District, India. The values were obtained during the pre-monsoon season at a soil depth of 10 cm, during the 12th week of their measurements. Lou et al. (2018) reported an upper value temperature for sand and gravel at about 20.2 °C at a depth of 120 m in Wuhan, China. The authors concluded that techno-economic feasibility of GHPS greatly depended on the geological properties and hydro-geological conditions of the site.

In Rampur District, Nepal, Poudel et al. (2012) observed a maximum soil temperature of 31 °C measured at a depth of 10 cm. The authors observed an increase in soil temperature in winter and a decrease at depths lower than 10 cm in summer season, concluding that solar radiation has a large influence over ground upper layers, while geothermal energy increased the soil temperature at larger depths in the winter season. Xing (2014) presented experimental data and a numerical model for soil temperatures at Los Lunas, New Mexico. The study showed a maximum soil (with vegetation) temperature of 34 °C at a depth of 5 cm in the arid and cold steppe climate. Xing (2014) computed an average temperature of 17.6 °C on soil covered with short grass in Puebla, Mexico.

Zhang et al. (2015b) studied the effects of grain size and finest content on thermal conductivity of three typical sands with high quartz content. The authors found that thermal conductivity of pure sands decreased as grain size declined and it was affected by the increase of number of physical contact points, thereby it caused an increment in thermal resistance between sand particles. Zhang et al. (2015b) also showed that porosity of 0.50 and fines content of 50 % caused an increase in thermal conductivity of sands with high quartz content ($k_{Ottawa\ 20/30}$ = 0.35 W/m K). A sand sample with porosity of 0.36 and the same percentage of fines content showed a decrease of thermal conductivity up to 0.17 W/m K. Moreover, the thermal conductivity of sands with uniform grain size decreased as grain size decreased, while for sands with nonuniform grain size, the thermal conductivity increased as a result of fine particles in sand pores. Thus, it was concluded that dry fine sands have lower thermal conductivity than coarse sands; however, higher thermal

conductivity can be achieved with low moisture content as a result of the particle size effect.

Yang et al. (2015) studied sand with 0% water content. Soil temperature dropped from 9.0 to 1.7 °C considering a time period of 10 years of operation, while for the soil moisture content of 0.15, 0.30 and 0.45, soil temperature dropped to 2.6 °C, 5.4 °C and 7.7 °C, respectively. You et al. (2017) stated that annual soil thermal imbalance used for GHPS located in cold regions occurs due to large accumulated soil heat extraction in winter and a small accumulated soil heat injection in summer season. The authors agreed that the large heat extraction from the soil at peak space heating loads also decreases the borehole outlet temperature in GHPS with vertical closed-loop. These soil conditions decrease the heating capacity of GHPS, thus increasing the number of boreholes and the installation cost. Furthermore, the highest average soil temperature of ground for non-coupled and coupled GHPS simulated with TRNSYS were found at 11.5 °C and 8.5 °C, respectively. You et al. (2016) concluded that soil thermal imbalance can be the cause of the following problems in GHPS performance: i) soil temperature decrease, ii) heating performance decay, iii) heating reliability decline, and iv) system failure. However, the main limitation of these studies is that soil moisture has been neglected in the analysis.

Bleicher and Gross (2016) reported that soil humidity had a direct influence on installation and operation in the heating mode of GHPS. Beier et al. (2011) used wet sand as soil to bury the U-tube of a GHPS; however, apart from considering soil's moisture content, the study did not consider factors such as grain size, and grain shape. Luo et al. (2016) specified the heat transfer rate of a borehole heat exchanger for closed-loop GHPS with saturated sand, 1,800 annual operation hours and in heating mode of around 65-80 W/m. The saturated sand had the second-high heat transfer rate in twelve common geological materials under the same system operation duration. The authors concluded that parameters such as grain size and soil moisture are connected to thermal conductivity of geological materials. According to the Department of Agriculture of the United States of America and the Connecticut Department of Energy and Environmental Protection, soil moisture content has a big influence over its thermal resistivity (US Department of Agriculture, 2016). Analyses have shown that high moisture contents have an effect on soil's low thermal resistivity. Alrtimi et al. (2016) concluded in their experimental investigation of Tripoli sand that the change of the thermal conductivity versus the moisture percentage can be given as a logarithmic function.

Meline and Kavanaugh (2017) concluded that soil moisture affects the heat flux in the upper end of boreholes in Vertical Geothermal Heat Exchangers; however, it is uncertain what takes effect at depths between 61 m or 152 m. The models currently being used in the aforementioned studies provided limited insight because they do not consider other important physical factors such as grain size, sand color and grain shape in their analysis.

Jin et al. (2017) classified the influence factors of soil thermal conductivity in three groups: the first group is the nature of soils, the second factor is the structural condition and the third influence is the physical condition. The nature of soils includes texture, mineral composition, shape and size of soil particles; the structural condition covers porosity and particle arrangement; finally, the physical condition is comprised by water content, temperature and pressure. Jin et al. (2017) also affirmed that the empirical and mathematical models have demonstrated an underperformance because it is difficult to describe all the material characteristics connected with the thermal conductivity of sands, such as the particle geometry, pore size distribution and the arrangement of the water bridges between grains. The authors suggested a theoretical model to compute soil thermal conductivity considering the effects of porosity, degree water saturation, average pore size, the nature of the respective interfacial interaction of the pore water and vapour phases with the solid phase at the pore wall surface, the pore structure and the material nature of all phases (solid, liquid and gas).

Zhang et al. (2017) indicated that water and quartz content had an effect on soil themal conductivity more than other factors such as gradation. The authors considered that quartz had an outstanding influence on soil thermal conductivity, having the highest thermal conductivity among soil minerals. Other factors such as size and shape decides grains packing and also have influence on soil thermal conductivity. An additional predominant factor is the number of contact point among dry soil grains which serve as bridges for heat flux. The study could not predict sand thermal conductivity with the Midttømme model due to lack of grain size data. Finally, the authors applied Chen (2008) model to predict sand thermal conductivity in GHPS installations; however, the theoretical model did not consider water content and grain size. Similarly, Zhang et al. (2015a) model can only be applied to compute sand thermal conductivity with high quartz content.

Wang et al. (2019) treated dry quartz sand (particle size range of 0.35 mm) with bacterial and cementation solutions and four cycles of Microbial-Induced Calcium Carbonate Precipitation technique (MICP). MICP-induced crystals $CaCO_3$ among sand grains

increased their physical contact points and the heat flow paths. Thermal conductivity of MICP-treated sands was increased from 8.12 W/m K to 15.50 W/m K, showing that the replacement of air by $CaCO_3$ worked as thermal bridge among sand grains.

To the best of the authors' knowledge, apart from the limited amount of studies considering sands as possible heat sources for GHPS, there is a lack of research that fully acknowledges the influence of factors such as grain size, shape and moisture content over sand's thermal behaviour. Therefore, the aim of this paper is threefold: i) conduct experiments in different sand samples under different conditions, ii) develop a mathematical model for sand temperature predicition and iii) apply the obtained outputs in annual simulations to understand its impact on GHPS performance.

This paper is organized as follows. First, the materials, sand samples and methods are described. Next, the obtained temperature results for each type of sand is shown, followed by the development of a mathematical model to predict sand temperature. Then, to validate the model, a comparison between empirical and modelled data as well as with other pre-established models is provided. Finally, the paper will illustrate the use of the measured data in a building simulation tool to study the performance of a generic GHPS, followed by discussion and conclusions.

2. Materials and Method

2.1 Experimental procedure and sand samples

The experiment was designed to measure the temperature of i) five different dry sand samples; ii) three wet sand samples; and, iii) three sand samples placed in three beakers covered with round glass. These sand types were chosen as heat sources because of their wide availability in many dry regions in the Americas, especially in Mexico, Colombia and the USA. Figure 1 illustrates a simple generic diagram of the sand-air heat exchange process.

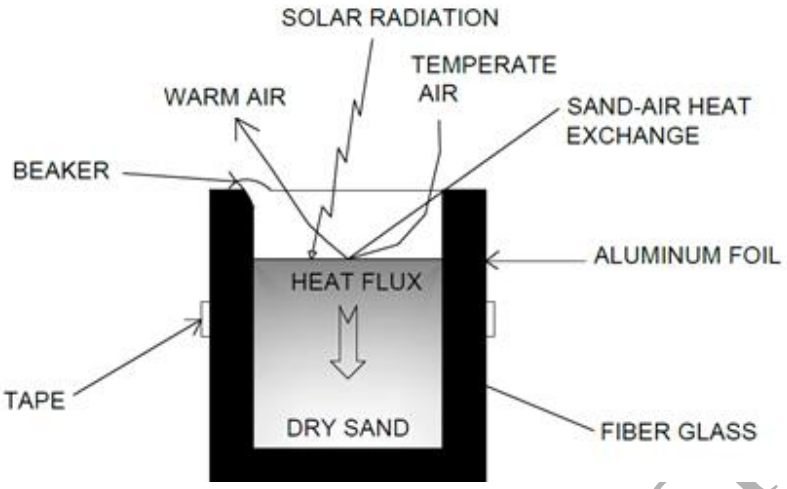

Figure 1. Diagram of sand-air heat exchange process.

The following steps were followed to develop the experiment:

2.1.1 Dry sand samples

1. Five sand samples were collected from different regions in Mexico: i) Cabo San Lucas, Baja California Sur (Northwest Mexico); ii) Puebla, Mexico (Central Mexico); iii) Veracruz, Mexico (Gulf of Mexico); iv) Puerto Marques, Guerrero (South Pacific coast); and v) Jilotzingo, Mexico State (Central Mexico).
2. Afterwards, the sand samples from Veracruz and Guerrero were washed and dried to remove fine clay.
3. *Porosity analysis:*

   The accumulated heat in the sand samples causes water vapor flow from the bottom to the top of the sand sample where the spaces between the grain's pores start to be filled with air and water. Pores in the sand sample with small grain size are smaller than pores in sand samples with larger grain size and thus the sand contains less water. Based on the estimations that the analysed sand mesopores are in the range between 1.7 to 300 nanometers, it is suggested to perform a nitrogen gas adsorption-desorption isotherm analysis according to the ASTM D-4365-13 (Test Method for Determining Micropore Volume and Zeolite Area of a Catalyst) (ASTM, 2013), either at 20-point or 40-point isotherm per sample (H. del

Rio-Moreno, personal communication, Jan 8th, 2019). Therefore, mercury porosimetry has been used to obtain porosity information in the size range of about 0.3 mm diameter up to about 360 mm and with compacted and sintered materials. In this experimental test, commercial instruments performed with maximum pressures of 414 MPa, forcing mercury to enter into the pores down to about 0.003 micrometers in diameter, potentially compressing the sand sample. If compression occurs, an appearance of mercury could be superimposed on the intrusion curve, leading to an error of mesopore size distribution.

4. *Sieve analysis:*

Sieve analysis was performed on the dry sand samples using an accurate balance and the ROT-TAP sieve shaker. The mass of the measured sample was set at 300 g each. The same method has been applied to measure the grain size distribution. Measurements showed that the sand sample from Baja California Sur, had a range of particle size of 300 mm with No. 50 ASTM. The sample from Puebla had a size of of 0.355 mm with No. 45 ASTM. The sample from Veracruz had a size of 0.600 mm with No. 30 ASTM, while the samples from Guerrero and Mexico State had sizes of 1.180 mm and 1.400 mm with Nos. 16 and 14 ASTM respectively. Figure 2 shows gradation curves according to ASTM designations for each sample.

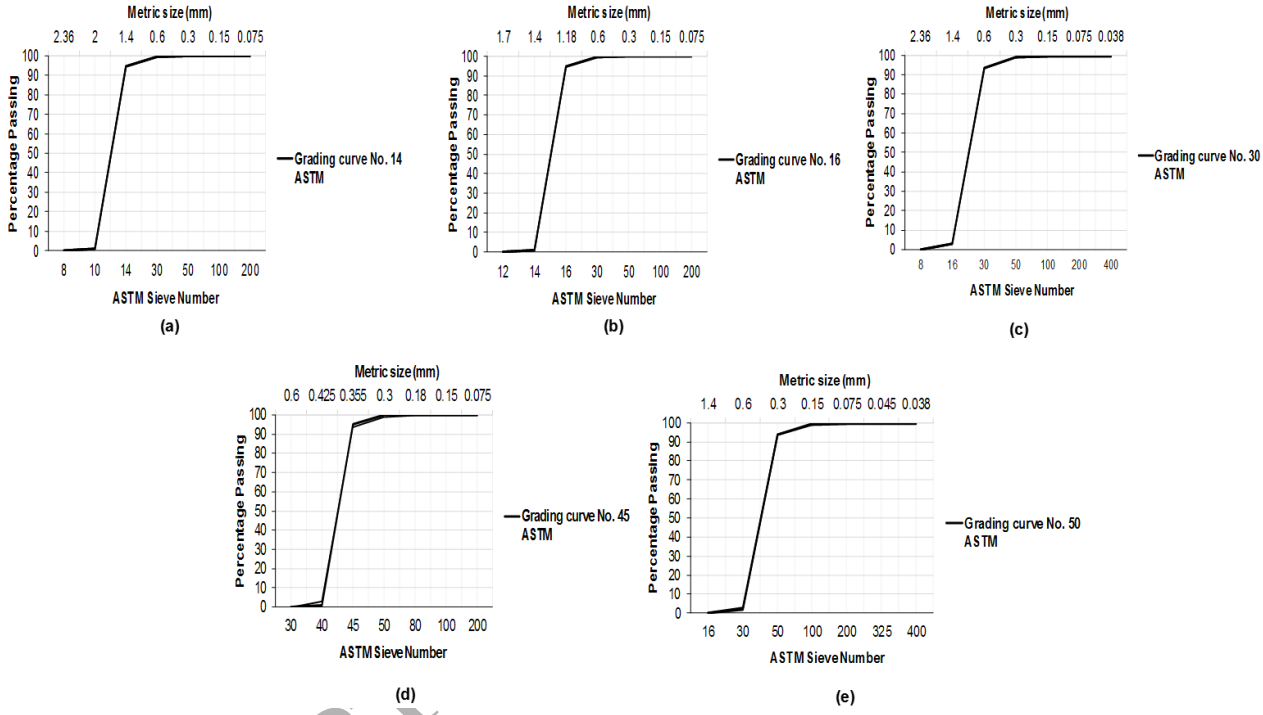

Figure 2. Gradation curves of (a) No. 14 ASTM, (b) 16 ASTM, (c) No. 30 ASTM, (d) No. 45 ASTM and (e) No. 50 ASTM designations.

The fineness modulus (3.03) was calculated as the sum of the cumulative percentage retained on selected sieves divided by 100. Figure 3 shows the granular characteristics of the five dry sand samples. These photomicrographs were taken with optical microscope (IROSCOPE) model WB-3. The dark grains observed in the sample with No. 30 absorb heat from solar radiation during the day and radiate it at night. The sub-angular and rounded grains of this dry sand acts as heat fins which capture and release heat from solar radiation faster than the angular, sub-angular and sub-rounded grains of other sand samples.

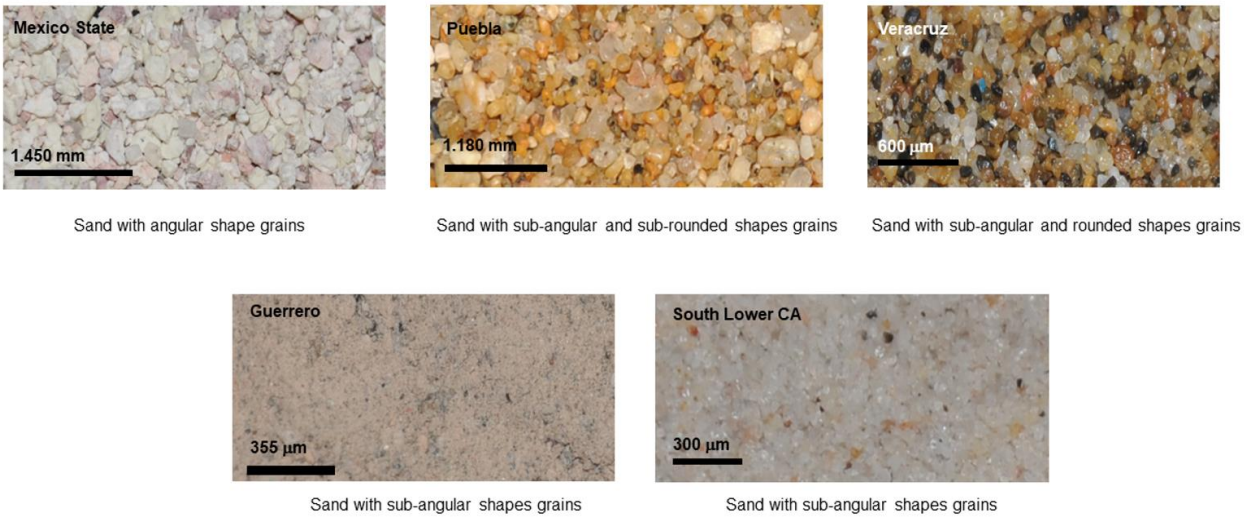

Figure 3. Colors and grain shapes of the five dry sand samples.

5. Five beakers were wrapped with glass fiber and aluminum foil (with a combined thickness of 2.54 cm) and fastened with adhesive tape to avoid heat loss. A Styrofoam panel board with a thickness of 1.27 cm was installed on the base of a metal grid to avoid heat flux between the building roof and the beakers bases.
6. Then, one liter of each sample of dry sand was placed in separate beakers.
7. The dry samples were weighed with a triple beam balance. Dry samples 1 through 5 weighed 1.310, 1.665, 1.060, 1.350 and 1.230 kg (these weights are the total weight of each beaker + sand).
8. A data logger (HOBO U12-012) and sensor (TMC1-HD) were installed to log the temperature on the surface of the dry sand sample with No. 50 ASTM. Additionally, three soil temperature sensors (TMC20-HD) were placed at a depth of 15 cm in the

dry samples with Nos. 50, 45 and 14 ASTM and were connected to a data logger (HOBO UX120). The program used to download the data was the HOBOware Pro 3.7.12. Two soil temperature sensors (SP03667) were connected to a data logger (WatchDog SP03685WD1) and were placed at a depth of 12 cm in the sand sample with No. 30 ASTM and 15 cm in the dry sand samples with Nos. 16 ASTM. Solar radiation was also logged with a silicon sensor pyranometer (LightScout, 3670i).

9. The measured temperatures in these dry sand samples were being downloaded each month with the program SpecWare 9 Basic. Temperature measurements were conducted between May 10th and July 20th, 2017.

Figure 4 shows a sketch of the cross section of the experimental setup with the beakers and the position of the sensors, while Figure 5 shows an actual picture of the experiment setup.

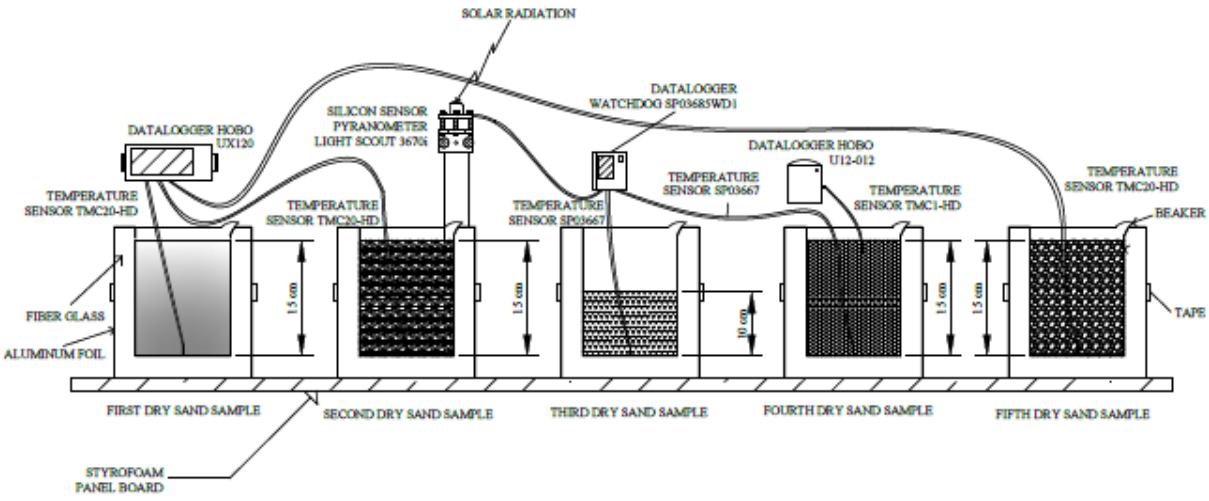

Figure 4. Sketch of the cross section of the experimental setup with the position of the sensors in the beakers.

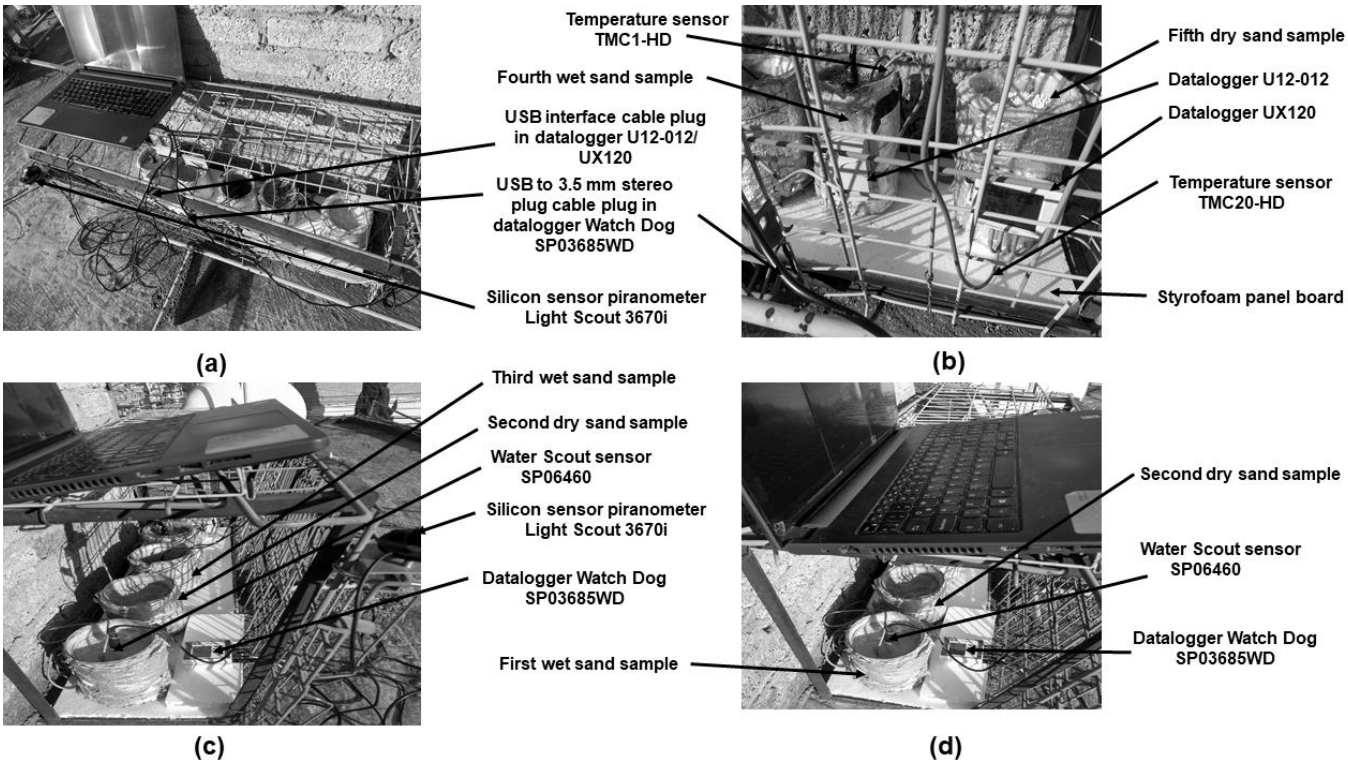

Figure 5. (a) Experiment setup, (b) zoom of dry sand with No. 14 ASTM, (c) description of experiment in the sand samples with Nos. 45 and 30 ASTM and (d) experiment in the sand samples with Nos. 50 and 45 ASTM.

10. The beakers were wrapped with glass fiber and aluminum foil with a combined thickness of 5 cm and covered with a round glass cover with a thickness 3 mm. The intention of the glass cover was to stop water loss from the beakers.
11. The beakers with the sand samples were placed on a panel of polyurethane with a thickness of 2.5 cm. Contacting parts of the beaker and glass cover were glued with silicon and sealed with high temperature silicon. Air between the surface of the sand samples and glass covers were removed and three beakers of sand samples have been sealed with silicone for launching a new logging period. The logging period was from November 12th, 2017 to April 14th, 2018.

2.2 Mathematical model derivation

Based on actual measurements, a mathematical model will be derived to predict the thermal behaviour of dry and wet sands to a depth of 15 cm. For this, the following steps are suggested:

1. First, based on the differential equation of second order suggested by Montheith and Unsworth (2013) that considers the second differential temperature (d^2T), the second differential depth (dz^2) plus differential temperature divided into differential time ($\frac{dT}{dt}$) and the negative thermal diffusivity ($-\alpha$), Eq. (1) can be defined as:

$$-\alpha \frac{d^2T}{dz^2} + \frac{dT}{dt} = 0 \quad (1)$$

where the thermal diffusivity in soil can be calculated assuming $\alpha_{soil} = \frac{k_{soil}}{\rho_{soil} SH_{soil}}$, where k_{soil} is thermal conductivity, ρ_{soil} is density and SH_{soil} is specific heat of soil.

2. After the differential equation is divided into $-\alpha$, the Laplace Transform is applied to solve it, thus a new equation is yielded. In this new equation (2), $T(0,t)$ is the temperature on time *t* to a depth of 0 m and t_e is bounded.

$$st_e - T(t,0) = \alpha \frac{d^2T}{dz^2} \quad (2)$$

With condition $T(t,0) = 0$

$$\frac{d^2T}{dz^2} - \frac{st_e}{\alpha} = 0 \quad (3)$$

3. A change of variable is applied to this equation obtaining a quadratic equation. Two solutions are yielded as result of solving this equation in function of variable λ. Eq. (4) shows this result:

$$T(z,t) = C_1 exp\left[z\left(\frac{\omega s}{2\alpha}\right)^{\frac{1}{2}}\right] + C_2 exp\left[-z\left(\frac{\omega s}{2\alpha}\right)^{\frac{1}{2}}\right] \quad (4)$$

According to Campbell and Norman (1998) ω is computed as follows:

$$\omega_{annual} = \frac{2\pi}{(365*24*3600)} \cong 2x10^{-7}\frac{rad}{s} \quad (4.1)$$

4. The general solution of differential equation will be the soil temperature at a depth *z*. In this step, the following considerations should be made: a boundary condition of temperature ($t_e = \frac{\omega}{2}$), $z \to \infty$ and the constant $C_1 = 0$. ω is the angular speed in a simple harmonic motion that simulates the thermal behaviour of the soil temperature. Eq. (5) shows this simplification:

$$t_e(z,t) = C_2 exp\left[-z\left(\frac{\omega s}{2\alpha}\right)^{\frac{1}{2}}\right] \quad (5)$$

5. The soil could be assumed with a finite depth and a surface temperature with sinuous variation. This sinuous variation is calculated as $\omega\Delta t + \varphi$, where $\omega\Delta t$ is the first angular displacement and φ the second angular position.
6. The annual temperature amplitude (A_0) on soil surface is calculated as the average of maximum daily temperature and minimum daily temperature.
7. Assuming the vertical component of annual temperature amplitude as A_{0y} and T_{sos} as soil surface temperature, equations (6) and (7) are obtained:

$$A_{0y} = A_0 \sin(\omega\Delta t + \varphi) \quad (6)$$

also

$$A_{0y} = T(0,t) - T_{sos} \quad (7)$$

8. The soil temperature at a depth of 0 cm and time t is calculated as the temperature measured on soil surface plus the result of multiplying the annual temperature amplitude per the sinuous variation. In this step, radians of sinuous variation is the result of adding the first position ($\omega\Delta t$) to the second position (φ) of sand. Δt is the difference between time t_1 and initial time t_0. Time t_0 is the first temperature with phase

constant of 34.6 days in the heating mode of GHPS. At time t_1 and t_2 the angular position φ is calculated as $\omega\ (t_2 - t_1)$. Eq. (8) shows this description.

$$t(0,t) = T_{sos} + \sin[\omega(t_1 - t_0) + \varphi] \quad (8)$$

9. By considering $T(t,0) = 0,\ T\ (0,t) = T_0$ and $\varphi = \omega(t_2 - t_1)$. Thus, the following equation is obtained:

$$\sin[\omega(t_1 - t_0) + \varphi] = \sin[\omega(t_1 - t_0)]\cos\varphi + \cos[\omega(t_1 - t_0)]\sin\varphi \quad (9)$$

10. By using Eq. (8) in Eq. (9), Eq. (10) is obtained:

$$T(0,t) = T_{sos} + A_0\{\sin[\omega(t_1 - t_0)]\cos[\omega(t_2 - t_1)] + \cos[\omega(t_1 - t_0)]\sin[\omega(t_2 - t_1)]\} \quad (10)$$

11. The Laplace transform is then applied to equation (10) that considers the soil temperature at a depth of 0 cm and time *t*, the annual temperature amplitude and the sinuous variation. A simplification of this equation has been done considering boundary condition of temperature $t_e(0,s)$ at a depth of 0 cm and function of s.

$$t_e(0,s) = L\{T(0,t)\} = \frac{T_{sos}}{s} + 2A_0\left[\frac{\omega s}{(s^2+\omega^2)^2}\right] \quad (11)$$

12. By substituting the second constant $C_2 = t_e(0,s)$ of step 5 in Eq. (11) and apply the inverse of Laplace transform to yield the equation of soil temperature in time *t* and a depth $z(T\ (z,t))$, this soil temperature is the result of adding the surface temperature with the multiplication of the annual temperature amplitude and the sinuous variation. Thus Eq. (12) is obtained.

$$t_e(z,t) = \frac{T_{sos}}{s} + 2\omega A_0\left[\frac{s}{(s^2+\omega^2)^2}\right] exp\left[-z\left(\frac{\omega s}{2\alpha}\right)^{\frac{1}{2}}\right] \quad (12)$$

Applying the inverse Laplace transform to Eq. (12) yields:

$$T(z,t) = T_{sos} + A_0 exp\left[-z\left(\frac{\omega}{2\alpha}\right)^{\frac{1}{2}}\right]\sin[\omega(t_1 - t_0) + \varphi] \quad (13)$$

13. Substituting $\omega = 2x10^{-7}\ \frac{rad}{s}$ in equation (13) yields:

$$T(z,t) = T_{sos} + A_0 exp\left[-z\left(\frac{\omega}{2\alpha}\right)^{\frac{1}{2}}\right]\sin[2x10^{-7}(t_1 - t_0) + \varphi] \quad (14)$$

14. Damping depth (*D*) is other parameter that can be include in equation (14). Monteith and Unsworth (2013) suggest the equation $\frac{1}{D^2} = \frac{\omega}{2\alpha}$. Substituting the mathematical expression in Eq. (14) yields:

$$T(z,t) = T_{sos} + A_0 exp\left(\frac{-z}{D}\right)\sin[2x10^{-7}(t_1 - t_0) + \varphi] \quad (15)$$

15. The second angular position of sand temperature (φ) is calculated as $\frac{-z}{D}$ because $\varphi = \omega(t_2 - t_1) = -\left(\frac{z_2 - z_1}{D}\right) = -\frac{z_2}{D} = -\frac{z}{D}$ with $z_1 = 0$ and $z_2 = z$. It is included as last variable in Eq. (15). Eq. (16) shows this substitution:

$$T(z,t) = T_{sos} + A_0 exp\left(\frac{-z}{D}\right)\sin\left[2x10^{-7}(t_1 - t_0) - \frac{z}{D}\right] \quad (16)$$

16. Changing $\frac{1}{D}$ in Eq. (16) by $\frac{\omega^{\frac{1}{2}}}{2\alpha}$, it yields:

$$T(z,t) = T_{sos} + A_0 exp\left[-z\left(\frac{\omega}{2\alpha}\right)^{\frac{1}{2}}\right]\sin\left[2x10^{-7}(t_1 - t_0) - z\left(\frac{\omega}{2\alpha}\right)^{\frac{1}{2}}\right] \quad (17)$$

17. Substituting the thermal diffusivity *(α_{soil})* , introduced in step 1, in the Eq. (17) and after a rearrangement, it yields the following equation:

$$T(z,t) = T_{sos} + A_0 exp\left[-z\left(\frac{\omega\varphi_{soil}SH_{soil}}{2k_{soil}}\right)^{\frac{1}{2}}\right]\sin\left[2x10^{-7}(t_1 - t_0) - z\left(\frac{\omega\varphi_{soil}SH_{soil}}{2k_{soil}}\right)^{\frac{1}{2}}\right] \quad (18)$$

18. Considering $\varphi_{soil} = \frac{m_{soil}}{V_{soil}}$ where m_{soil} [kg] and V_{soil} [m^3] are mass and volume of soil, respectively. V_{soil} is be the sum of water volume and soil volume in case of wet sample and air volume and soil volume in case of dry sample.

19. Substituting φ_{soil} by $\frac{m_{soil}}{V_{soil}}$ in Eq. (18) and after rearranging the equation, it yields:

$$T(z,t) = T_{sos} + A_0 exp\left[-z\left(\frac{\omega m_{soil}SH_{soil}}{2k_{soil}V_{soil}}\right)^{\frac{1}{2}}\right]\sin\left[2x10^{-7}(t_1 - t_0) - z\left(\frac{\omega m_{soil}SH_{soil}}{2k_{soil}V_{soil}}\right)^{\frac{1}{2}}\right] \quad (19)$$

20. Computing the soil volume as $V_{soil} = \frac{\pi}{6}\left(\frac{d_G}{1000}\right)^3 n$ where d_G is grain size and n is the amount of grains. The grain size is the one measured in sieve analysis (section 2.1, step 4) and is calculated on division of grain volume and volume occupied by soil in beaker. Soil grain is considered with spherical shape and its volume is also calculated with the results of sieve analysis.

21. Replacing V_{soil} in Eq. (19), the derived mathematical model is shown in Eq. (20).

$$T(z,t) = T_{sos} + A_0 exp\left\{-z\left[\frac{6\omega m_{soil}SH_{soil}}{2k_{soil}n\pi\left(\frac{d_G}{1000}\right)^3}\right]^{\frac{1}{2}}\right\}\sin\left\{2x10^{-7}(t_1 - t_0) - z\left[\frac{6\omega m_{soil}SH_{soil}}{2k_{soil}n\pi\left(\frac{d_G}{1000}\right)^3}\right]^{\frac{1}{2}}\right\} \quad (20)$$

To derivate the necessary sand model, Monteith and Unsworth (2013) suggest an analytical model to calculate heat flux in soil as a function of thermal conductivity, depth and soil temperature variation. They also suggested that the difference between heat flux at depth *z* and any thin layer of thickness *dz* could be written with Fourier's partial differential equation. Eq. (21) calculates the volumetric specific heat of soil defined as the product of density ρ_{soil} [kg/m^3] and specific heat SH_{soil} [J/ kg K].

$$\rho_{soil} SH_{soil} = \rho_s SH_s x_s + \rho_l SH_l x_l + \rho_g SH_g x_g = \sum(\rho SH x) \quad (21)$$

Where the subscripts *s*, *l*, and *g* are the solid, liquid, and gaseous components of soil and *x* is the volume fraction of each component of it. Thermal conductivity was defined by Montheith and Unsworth (2013) *as* $k_{soil} = \alpha_{soil} \rho_{soil} SH_{soil}$ [W/m K]. Cengel (2004) proposed a values interval from 0.2-1.0 W/m K for sand.

Fourier's partial differential equation is modified with thermal diffusivity as follows:

$$\frac{dT}{dt} = \alpha \frac{d^2T}{dz^2} \quad (22)$$

When the Laplace transform is applied to solve Eq. 22, a variation of Eq. (13) is obtained. This includes a time interval of $\varphi = t_2 - t_1$ as showed in Eq. (23).

$$T(z,t) = T_{ss} + A_0 exp\left[-z\left(\frac{\omega}{2\alpha}\right)^{\frac{1}{2}}\right] \sin\{\omega[(t_1 - t_0) + (t_2 - t_1)]\} \quad (23)$$

Where T_{ss} is the sand surface temperature, in Celcius, A_0 is daily average amplitude that is calculated as the addition of daily maximum temperature and daily minimum temperature divided by two, in Celcius, $t_1 - t_0$ is the difference of time between initial time (t_0) and subsequent time $(t_2 - t_1)$, which is considered as an interval of 900 seconds.

Substituting the value of ω into sine, Eq. (24) gives:

$$T(z,t) = T_{ss} + A_0 exp\left[-z\left(\frac{\omega}{2\alpha}\right)^{\frac{1}{2}}\right] \sin\{2x10^{-7}[(t_1 - t_0) + (t_2 - t_1)]\} \quad (24)$$

Substituting damping depth of Eq. (15) in Eq. (24) gives:

$$T(z,t) = T_{ss} + A_0 exp\left[\frac{-z}{D}\right] \sin\{2x10^{-7}[(t_1 - t_0) + (t_2 - t_1)]\} \quad (25)$$

Where t_1 and t_2 are the times that the temperature reaches a temperature at depth z_2 and a minimum at depth z_1. All conditions of Eq. (16) and the change of D in Eq. (17) can be used in Eq. (25). By doing this, the following equation is obtained:

$$T(z,t) = T_{ss} + A_0 exp\left[-z\left(\frac{\omega}{2\alpha}\right)^{\frac{1}{2}}\right] \sin\left\{2x10^{-7}\left[(t_1 - t_0) - z\left(\frac{\omega}{2\alpha}\right)^{\frac{1}{2}}\right]\right\} \quad (26)$$

Changing the equation of thermal diffusivity of Eq. (1) by thermal diffusivity of sand, the Eq. (26) can be modified as follows:

$$T(z,t) = T_{ss} + A_0 exp\left[-z\left(\frac{\omega\rho_s SH_S}{2k_s}\right)^{\frac{1}{2}}\right] \sin\left\{2x10^{-7}\left[(t_1 - t_0) - z\left(\frac{\omega\rho_s SH_S}{2k_s}\right)^{\frac{1}{2}}\right]\right\} \quad (27)$$

Where ρ_s [kg/m^3] is the density, and SH_S [J/kg°C] is the specific heat of the sand.

Later in this study, the derived model is compared with other models to illustrate the difficulty in predicting sand temperatures with sand size No. 30 ASTM. The model is also compared with the temperature measurements of dry sand sample with No. 16 ASTM and

wet sand sample with No. 50 ASTM. This comparison aims to demonstrate the reliability of the derived mathematical model to predict the temperature of two sand types with more accuracy.

3. Temperature measurements

3.1 Temperatures of the dry sand samples

Figure 6 shows the profile of high temperatures of the sand samples from May 22nd to 28th, 2017. All dry sand samples reached temperatures of over 40 °C. As shown, the grain size has a direct influence on the dry sand temperature. For example, the temperature profile of the dry sand sample with No. 50 ASTM is higher than that of the dry sand samples with Nos. 14, 16 and No. 45 ASTM. However, the highest measured temperature was 47.20 °C reached by the dry sand sample with No. 30 ASTM. This temperature was logged at 15:00 h on May 23rd, 2017.

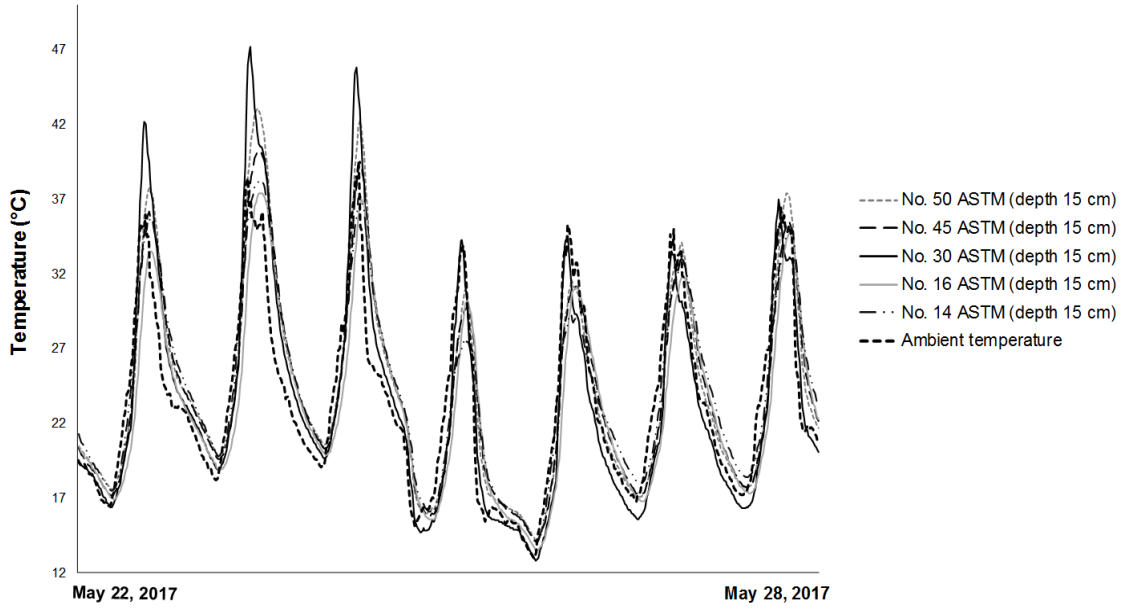

Figure 6. Highest temperatures logged in the five dry sand samples at depth of 15 cm (Ambient temperature as dotted dark line).

Figure 7 shows that the No. 30 ASTM sample logged the lowest temperatures compared to the rest. The lowest measured temperature was 11.9 °C at 7:45 h on June 15th, 2017.

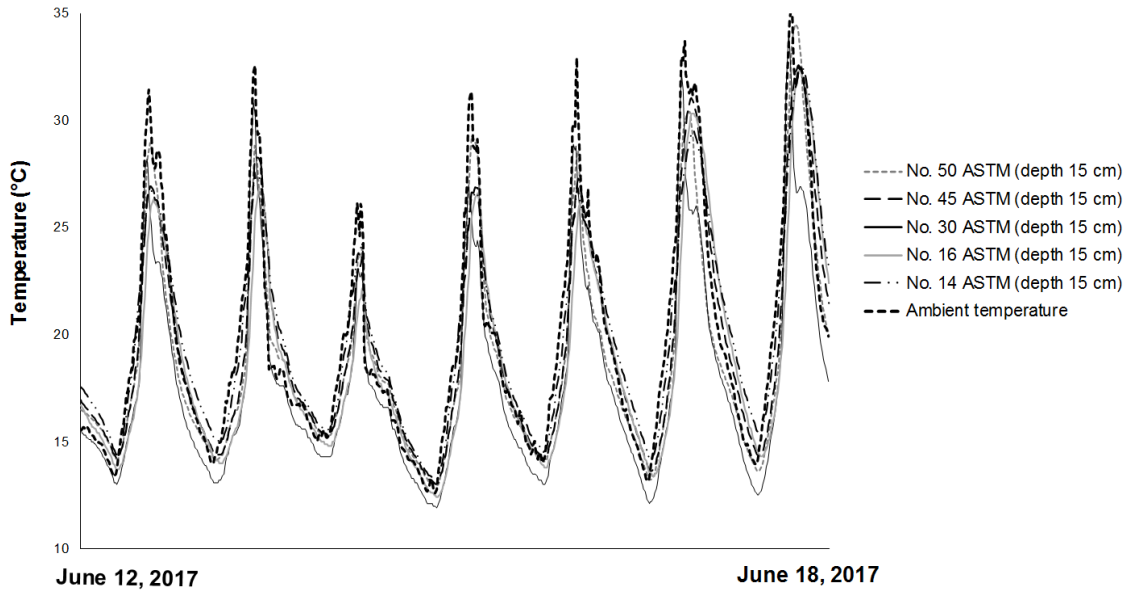

Figure 7. Lowest temperatures logged in the five dry sand samples at depth of 15 cm (ambient temperature as dotted dark line).

Solar radiation was also logged and plotted against sand temperatures. Figure 8 shows the profile of temperatures in the No. 16 ASTM dry sample as well as solar radiation values for July. This sand sample was selected because: i) it can be easily found on the coast of the Mexican Pacific Ocean, ii) it has a large amount of quartz grains that can transfer the heat flux of solar radiation; iii) and allows to establish a comparison of behaviour between the temperatures of dry sand with larger grain and the temperatures of wet sand with small grain size as well as the derived mathematical model.

Figure 8 shows that an increase in the solar radiation causes an increase in the temperature of the sample. On July 18th, a radiation 1,099 W/m^2 was logged as the No. 30 ASTM and No. 16 ASTM sand samples logged 28.20 °C and 33.60 °C, respectively. After thirty minutes, the No. 16 ASTM sand sample logged 34.70 °C, the highest recorded temperature for the sample in July. One hour after the maximum solar radiation, the No. 30 ASTM sample logged 28.80°C (+0.60 °C), the highest temperature for the sample in this month. Dry sand with large grain size rejected the heat of solar radiation in smaller time than dry sand with small grain size. Also, dry sand with large grain size logged higher temperature than dry sand with small grain size for similar solar radiation.

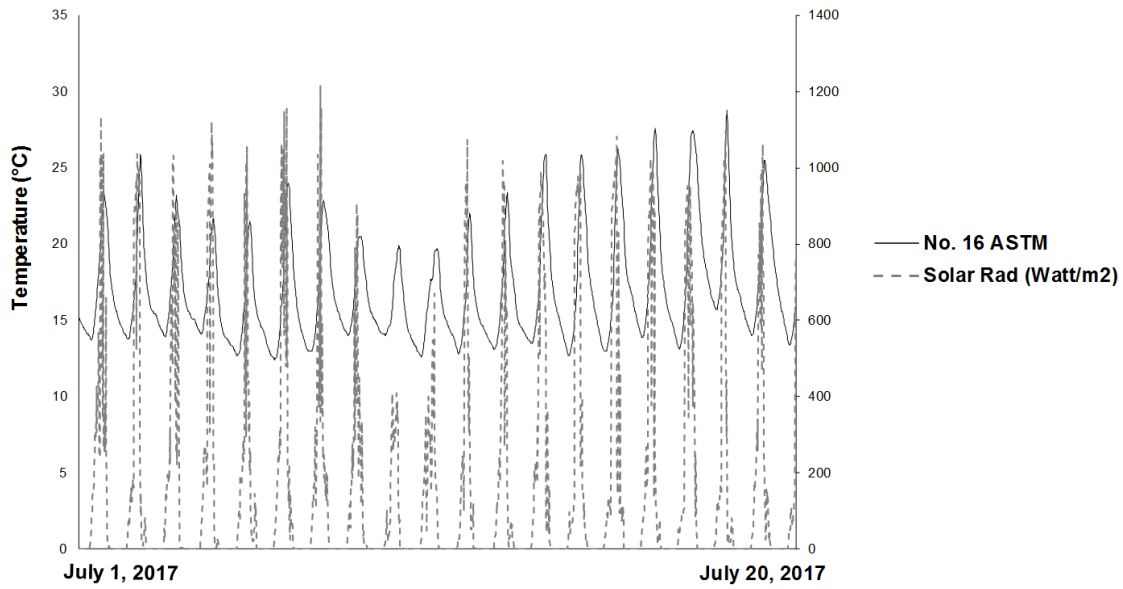

Figure 8. Temperatures of the No. 16 ASTM sand sample and solar radiation.

Similar outputs show that sand with range of particle size of 0.300 mm (No. 50 ASTM) logged similar temperatures to coarse grain samples, but in less time. The thermal behaviours of sands with ranges of particles sizes of 0.300 mm (No. 50 ASTM) and 0.600 mm (No. 30 ASTM) suggest burying the closed-loop of GHPS in sand with fine grains of quartz at day and change the water flow to other closed-loop that it is buried in sand with fine grains of quartz and clay at night.

3.2 Temperatures of the wet sand samples

The temperatures of the three wet sand samples with No. 50, 30, and 16 ASTM were logged and compared. The log period began at 18:30 h on August 14th and ended at 10:30 h on November 10th, 2017. Figure 9 shows the highest temperature for the sample with No. 16 ASTM was logged at 38.75 °C, at 16:15 h on October 20th, 2017. On October 19th, 2017 the wet sand sample with No. 30 ASTM reached its highest logged temperature (44.06 °C), and at 15:30 h the wet sand sample with No. 50 ASTM reached its highest temperature (39.05 °C). A shown in this figure, the temperature in the wet sand sample with larger grain size was lower than the temperatures in wet sand samples with smaller grain size. Also, the temperatures in the wet sand sample with No. 30 ASTM were always

higher than the temperatures in wet sand samples with No. 16 and No. 50 ASTM. Note that the sample with No. 30 ASTM has much darker grains of quartz combined with angular shapes.

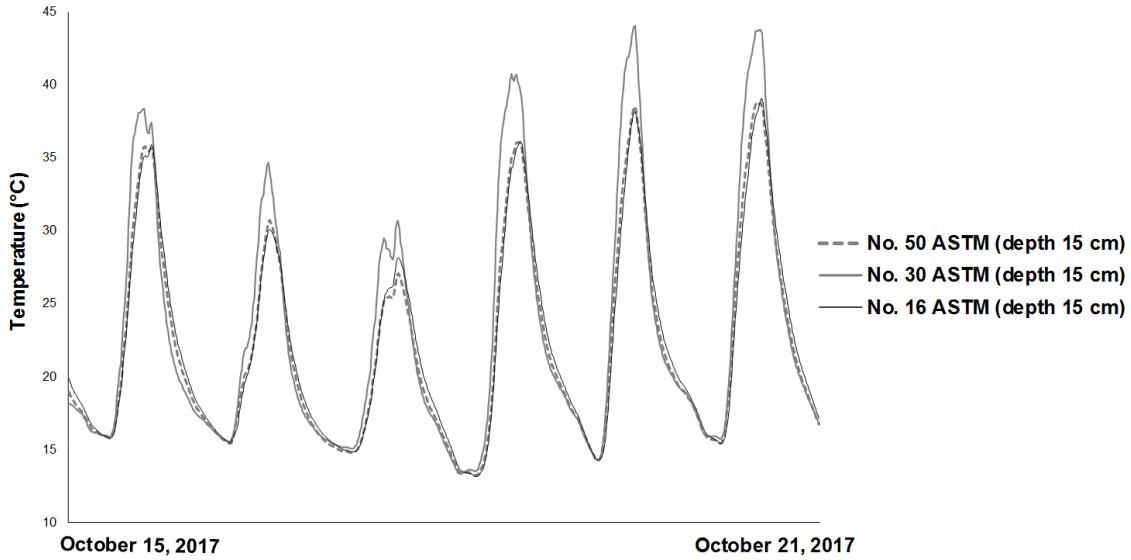

Figure 9. Temperatures of three wet sand samples at depth of 15 cm from October 15 to 21, 2017.

The wet sand with No. 16 ASTM reached the lowest temperature of 10.43 °C at 7:45 h on September 11th, 2017 (Figure 10).

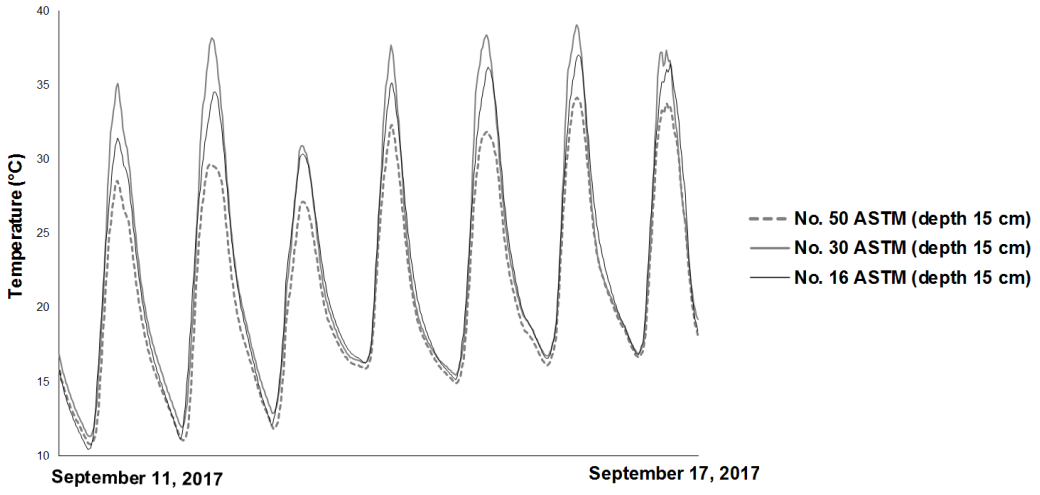

Figure 10. Temperatures of three wet sand samples at depth of 15 cm from September 11th to 17th, 2017.

3.3 Moisture content

Figure 11 shows the decrease of moisture content of the three wet sand samples (No. 16, 30, and 50 ASTM) between October 1st and October 28th, 2017. During the day, the water evaporated from the wet sand samples.

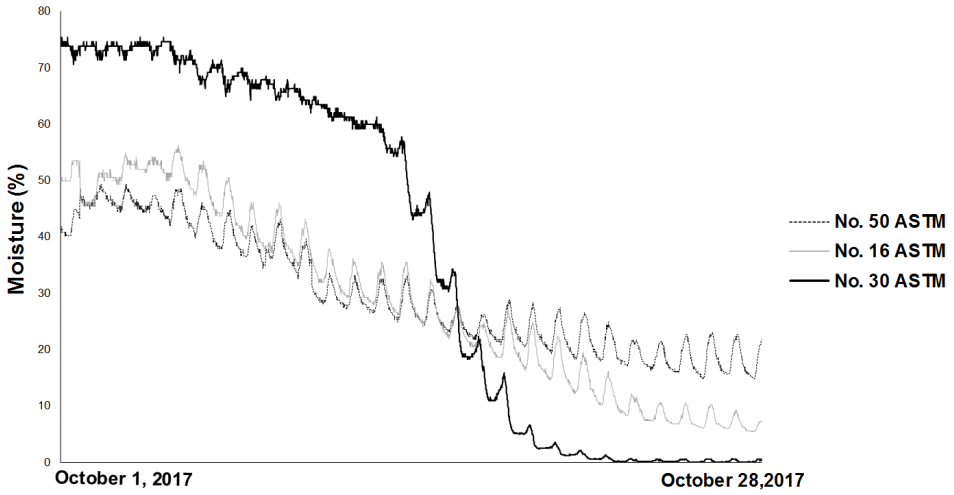

Figure 11. Change in moisture content of three wet sand samples in October 2017.

The wet sand sample with No. 16 ASTM had combination of clay grains with quartz grains and the wet sand sample with No. 30 ASTM only had quartz grains. Quartz grains were a better heat conductor than clay grains. Wet sand samples with Nos. 16 and 50 ASTM had 24.9 % and 16.20 % moisture, respectively. The wet sand sample with No. 50 ASTM logged the highest moisture percentage of the three wet samples at the end of the measured period. This is because pores in fine grained sands are smaller than pores in coarse grained and, consequently, water vapor flows more easily in sand with large grain size. During the day, the No. 50 ASTM sand sample increased its moisture content by 6 % compared to night time. Figure 10 also shows that the wet sand sample with No. 30 ASTM lost 75 % of its moisture in twenty-eight days and was reduced to near zero over the duration of the experiment. Therefore, the sand with the highest temperature lost all its water in one month during the autumn season in the analysed region (Central Mexico). By October 10th, 2017 all water evaporated from the wet sand sample with No. 30 ASTM. These physical effects could be caused for the following reasons in this wet sand sample:

i. Grains with sub-angular shapes have been accommodated in very close way and absorbed large amounts of heat.
ii. Due to large amount of dark color grains, they absorbed more heat and evaporated the water.
iii. The space between the sub-angular shapes grains has been reduced and it contained little water amount.

The other wet sand samples were reduced only by 25 % and 10 % moisture respectively, explaining the moisture holding capacity of clay grains.

3.4 Temperatures of sand samples contained in beakers and glass covered

The highest logged temperatures in the sand sample with No. 50 ASTM was 43.45 °C, measured on March 4th, 2018. Temperatures in samples with Nos. 30 and 16 ASTM were 51.42 °C, and 43.16 °C respectively, logged at 15:45 h on April 4th, 2018. Maximum temperatures in our sand samples with a glass cover were higher than the maximum temperature of 37.5 °C in wet sand at depth 13 cm measured in an experiment (at time 50 h) by Garcia-Padron and Loyd (2002). The initial percentages of moisture in the sand samples were 20.9 %, 0 % and 31.9 %, respectively. Table 1 shows temperature, moisture percentage and direct solar radiation for two sand samples logged on November 15th, 2017.

Table 1. Temperature and moisture percentage of two sand samples with glass covers on November 15, 2017.

		Range of particle size (ASTM designations)			
		No. 30	**No. 16**	**No. 30**	**No. 16**
Date and time	**Sol. Rad. (W/m^2)**	**Temp.(°C)**	**Temp.(°C)**	**Moist. (%)**	**Moist. (%)**
15-11-2017 00:00	0	15.33	16.43	12.20	24.40
15-11-2017 02:00	0	13.31	14.06	11.90	24.00
15-11-2017 04:00	0	11.58	12.12	11.60	23.10

15-11-2017 06:00	0	10.16	10.64	10.90	22.70
15-11-2017 08:00	48	9.82	9.99	10.60	22.30
15-11-2017 10:00	511	18.01	18.25	13.60	25.30
15-11-2017 12:00	722	29.43	29.64	17.00	28.40
15-11-2017 14:00	668	38.37	37.62	19.60	31.30
15-11-2017 16:00	334	41.92	40.12	20.50	31.90
15-11-2017 18:00	1	33.09	34.24	17.40	29.70
15-11-2017 20:00	0	24.30	26.02	14.90	27.10
15-11-2017 22:00	0	19.39	20.93	13.20	25.80

Table 1 also shows the relationship between the highest temperature of the sand samples and the highest moisture percentage which were logged at 16:00 h. Direct solar radiation of 437 W/m^2 as logged by our data logger (SP03685WD1) at 15:30 h on November 18th, 2017 was higher than the 180 W/m^2 reported in the study of Garcia-Padron and Loyd (2002). This shows the direct influence of solar radiation and a glass over the maximum temperature of dry sand. The glass covers also avoided the total loss of water in sand samples. The moisture variation in the two sand samples could be due to an imperfect manner of sealing the beakers.

3.5 A comparison of samples in the three experiments

The temperatures in the sand sample with No. 30 ASTM for all three experiments were logged between May 10th, 2017 and April 14th, 2018. As shown in Table 2, when the sample was contained in beakers and covered by glass, it logged the highest temperature, followed by the dry sample and the wet sample.

Table 2. Data of maximum measured temperature in the sand experiment at a depth of 0.15 m.

Sample type	**ASTM designation**	**Moisture (%)**	**Maximum measured temp. (°C)**	**Date**
Dry	30	0	47.20	May 23rd, 2017

Wet	30	4.6	44.06	October 19th, 2017
Glass covered sample	30	0	51.42	April 4th, 2018

The dry sample had the lowest temperature of all analyzed experiments, reaching 11.90 °C at 7:45 h on June 15, 2017. In this experiment, no influence was found of the sand mass over its temperature. It might be that the effects of color, grain shape, and grain size simply overwhelm the mass factor.

The highest temperature of 51.42 °C that was logged in the experiment in the dry sand sample with No. 50 ASTM. This temperature was caused by the following factors:

- High quartz content;
- Fine-grained sand;
- Large amount of dark grains;
- Vacuum space;
- Sub-angular and rounded grains;
- Glass cover retarded the heat loss in the sand sample;
- And moisture percentage of 0 %.

3.6 Mathematical model of sand

Based on the derivation of the mathematical model shown in section 2.2, a model has been developed to predict the thermal behaviour of dry and wet sands to a depth of 15 cm. In this study, it is assumed that for the No. 50 ASTM sand α is 4.26 x10^{-7} m^2/s, for the No. 30 ASTM covered wet sand sample is 3.38 x10^{-7} m^2/s and for the No. 16 ASTM dry sand sample is 2.54 x 10^{-7} m^2/s. The grain diameter (d_G), analysed by sieve analysis and the number of grains (n), was calculated at 68.97 x 10^6 grains, 3.98 x10^6 and 3.93 x 10^5 grains in the case of the No. 50, 30, and 16 ASTM samples, respectively. By calculating the sand volume (V_s) and making the replacement in Eq. (27) yields the following model:

$$T(z,t) = T_{ss} + A_0 exp\left\{-z\left[\frac{6\omega m_s S H_s}{2k_s n\pi\left(\frac{d_G}{1000}\right)^3}\right]^{\frac{1}{2}}\right\}\sin\left\{2x10^{-7}(t_1 - t_0) - z\left[\frac{6\omega m_s S H_s}{2k_s n\pi\left(\frac{d_G}{1000}\right)^3}\right]^{\frac{1}{2}}\right\} \quad (28)$$

This derived mathematical model is similar to Eq. (20) and includes the grain size of a sand sample. This new model can be used to predict the temperatures in the No. 30 ASTM and No. 16 ASTM dry sand samples as well as in the No. 50 ASTM wet sand sample.

4. Results

4.1 Model validation and empirical data comparison

Table 3 shows the predictions from the derived mathematical model compared to the measured temperatures in three sand samples, validating the model's outputs. Temperature sensor buried in the No. 16 ASTM sand sample betweem May 10th and July 20th, 2017, was changed and buried in the No. 50 ASTM wet sand sample between August 12th and October 20th, 2017. At the last period of log, the temperature sensor was changed again and buried in the No. 30 ASTM dry sand sample of beaker with glass cover. It was carried out to measure and to log the surface temperatures of sand samples with different ranges of particle sizes and percentages of moisture in the three stages of the experiment. For that reason, the measurements of temperature of the other two sand samples are not showed in the predictions of the derived mathematical model in Table 3.

Table 3. Comparison between temperatures computed with the derived mathematical model and the temperatures logged by the data loggers in the sand samples with Nos. 50, No. 30 and No. 16 ASTM.

Sample type	**ASTM Number**	**Range of particle size (mm)**	**Measured temp. (°C)**	**Date (2017)**	**Time of log (h)**
Wet	50	0.300	15.91	August 13	6:30
Dry	30	0.600	44.93	November 16	14:30
Dry	16	1.180	20.00	May 18	4:45
Sample type		**Range of particle size (mm)**	**Calculated temp. (°C)**	**Date (2017)**	**Time of log (h)**
Wet	50	0.300	15.91	August 13	6:30
Dry	30	0.600	44.92	November 16	14:30
Dry	16	1.180	20.04	May 18	4:45

A comparison between a time-series outputs from the derived mathematical model and the measured temperature of the No. 16 ASTM (particle size of 1.180 mm) dry sand sample (from May 16th to 31st, 2017) is shown in Figure 12. Figure 13 shows the same for the No. 50 ASTM (particle size 0.300 mm) wet sand sample (from August 12th to 23rd, 2017) and Figure 14 shows the No. 30 ASTM (particle size of 0.600 mm) dry sand sample contained in beaker with glass cover (from November 12th to 27th, 2017).

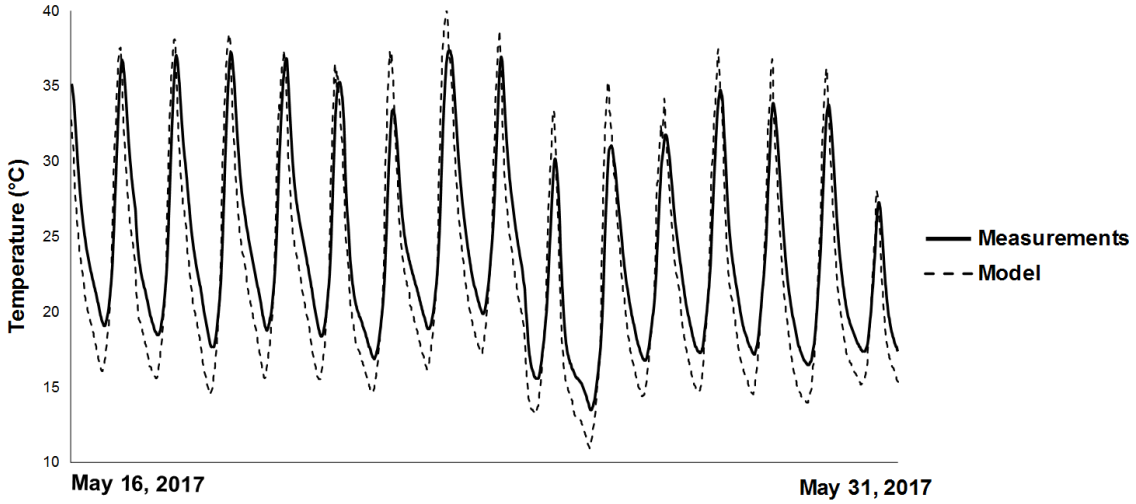

Figure 12. Comparison of the results from the derived mathematical model and temperatures of the dry sand sample with No. 16 ASTM.

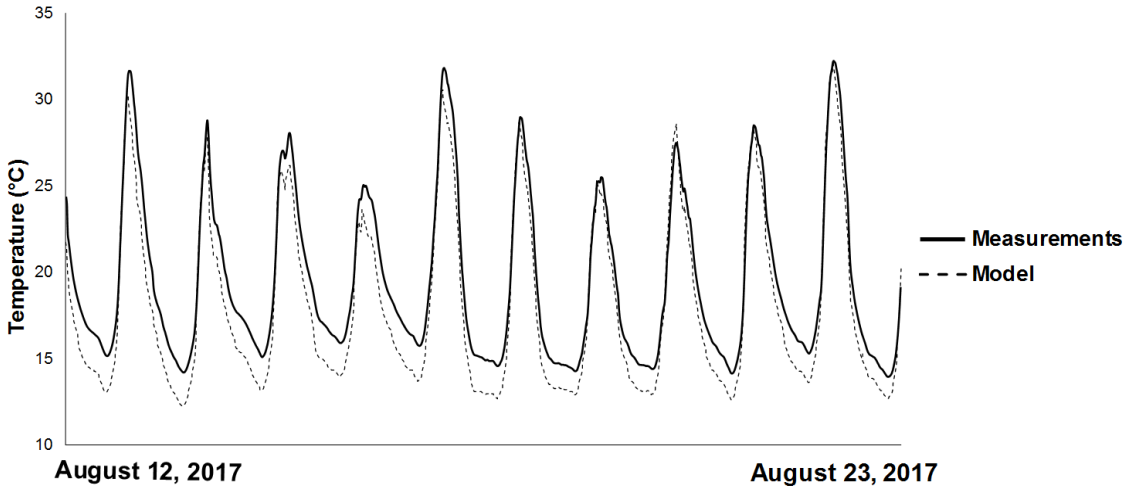

Figure 13. Comparison of the results from the derived mathematical model and temperatures of wet sand sample with No. 50 ASTM.

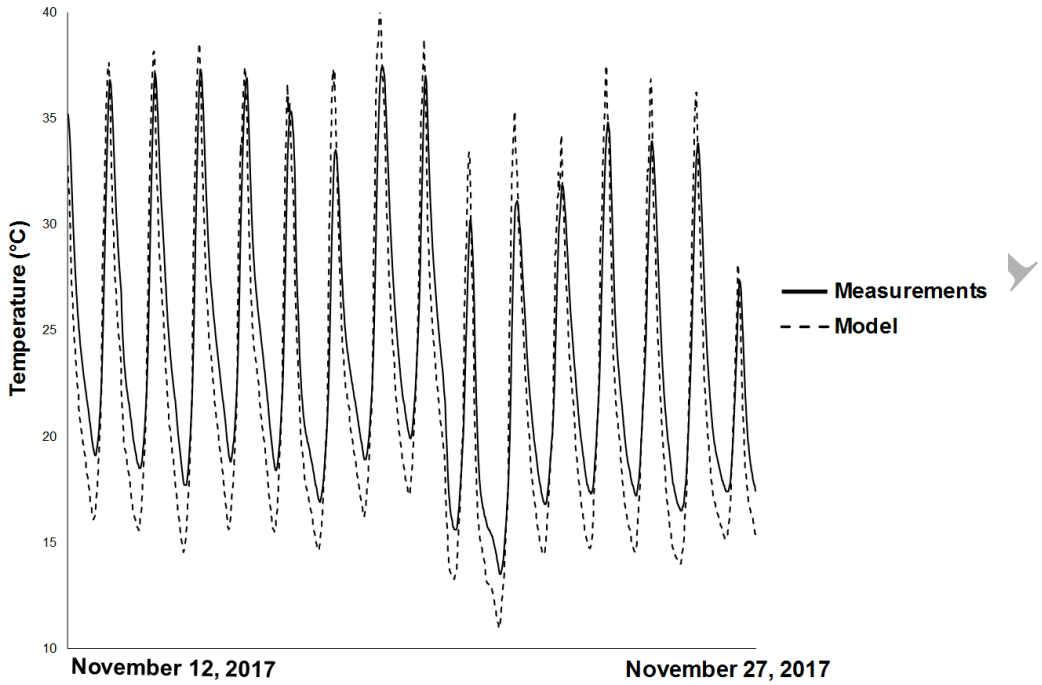

Figure 14. Comparison of the results from the derived mathematical model and temperatures of dry sand sample with No. 30 ASTM contained in beaker with glass cover.

Thermal conductivity in the No. 50 ASTM, No. 30 ASTM, and No. 16 ASTM sand samples were found at 0.70 W/m K, 1.00 W/m K and 1.00 W/m K, respectively. These values act as an input in the derived mathematical model. For computation of temperature in the No. 16 ASTM sand sample, air volume of $3x10^{-7}$ m^3 between grains was also assumed.

As shown in Figures 12, 13, 14 and table 3 the results of the model correlated much better with the temperature profile of the wet sand sample with No. 50 ASTM contained in beaker with glass cover than the temperature profile of dry sand samples No. 30 ASTM and No. 16 ASTM.

Anderson et al. (1999) described a method to calculate the Median Absolute Deviation (MAD). This value is the average absolute values of prediction errors and is computed as follows:

$$MAD = \sum \frac{|T_s - T_{DMM}|}{N} \quad (29)$$

Where T_s is the measured sand temperature (°C), T_{DMM} is the temperature of sand sample that was computed to the derived mathematical model (°C) at the same time and N is the number of measurements of period. Table 4 shows the results of MAD that have been computed for the analysed samples.

Table 4. Calculation of MAD in the sand samples with Nos. 50, 30 and 16 ASTM.

Sand sample	$\|T_s - T_{DMM}\|$	**N**	**MAD**
No. 50 ASTM (wet)	1,647.96	1,026	1.59
No. 30 ASTM (dry)	3490.87	1,437	2.43
No. 16 ASTM (dry)	3,952.66	1,463	2.70

4.2 Comparison with other mathematical models

In this section, a comparison between the measurements of temperature of sand No. 50 ASTM and different mathematical models has been made. Table 5 shows the equations of the considered models.

Table 5. Soil temperature equations from different models

Authors	**Equation**
Jutglar et al. (2011)	$T = \frac{G}{2kz^2} + C_z + T_0$
Monteith and Unsworth (2013)	$T(z,t) = T + A(z)\sin\left(\omega t - \frac{z}{D}\right)$
Equation proposed by Labs (1989) and Mihalakakou et al. (1992)	$T(z,t) = T_m - A_s exp\left[-z\left(\frac{\pi}{365\alpha}\right)^{\frac{1}{2}}\cos\left\{\frac{2\pi}{365\left(t - t_0 - \frac{z}{2\left(\frac{365}{\alpha\pi}\right)^{\frac{1}{2}}}\right)}\right\}\right]$
Givoni (Baruch 1994, cited by Derradji and Aiche 2014)	$T_s = T - A_0\exp(-zF)\sin(0.986t - 122 - Lz)$

Measured temperature data was put into these models to illustrate that the mathematical models of soil temperature find it difficult to predict the high and low temperatures of sand. These comparisons and the results computed with the derived mathematical model are shown in Figure 15.

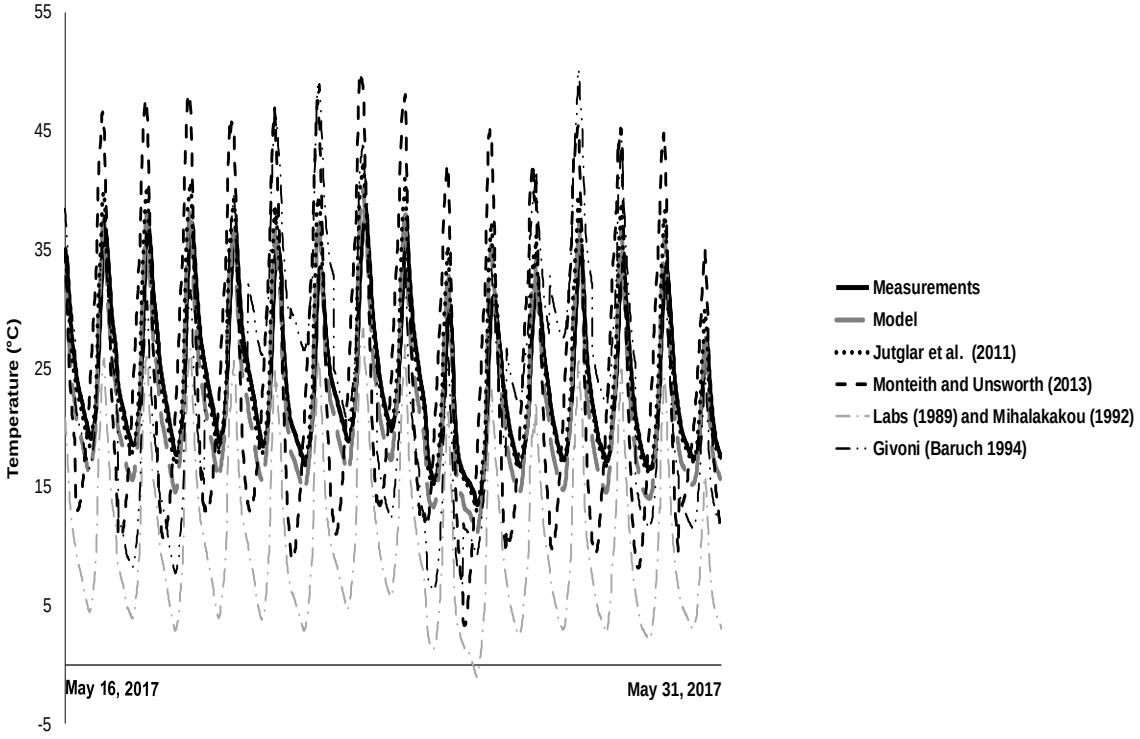

Figure 15. Comparison of the results of sand sample with No. 50 ASTM (grain size 0.300mm) temperature measurements with the derived mathematical model and other different models.

Although the results of the model of Jutglar et al. (2011) agree with some low temperatures from the sand sample, their equation predicted higher temperatures than the actual logged temperatures. However, of all mathematical models reported here, their model produced results that where the closest to the maximum temperatures logged in this sample.

The same method to compute the MAD can be applied to the models from Table 5 to compare with the measurements of the No. 50 ASTM wet sample. The obtained results are the following:

- MAD of Jutglat et al. (2011) model = 5.59
- MAD of Monteith and Usworth (2013) model = 8.20
- MAD of Labs (1989) and Mohalakakou (1992) model = 8.49
- And MAD of Givoni (1994) = 10.28

The MAD of the derived mathematical model is lower than the MAD of the Jutglar et al. (2011) model (1.59 against 5.59). This study's MAD is also lower compared to the rest of models.

4.3 Comparison with Kavanaugh and Rafferty model

A further comparison was made with the model proposed by Kavanaugh and Rafferty (2014) and the measured monthly average temperatures of the dry sand sample with No. 16 ASTM (1.180 mm grain size) (for the period from May 10th to October 31st, 2017). Some variables from the Kavanaugh and Rafferty model spreadsheet (GroundTemp. and ResIP-SI14 software) are shown in Figure 16. The thermal conductivity of sand is assumed at 2.0 W/m°C and its specific heat at 0.797 kJ/kg°C.

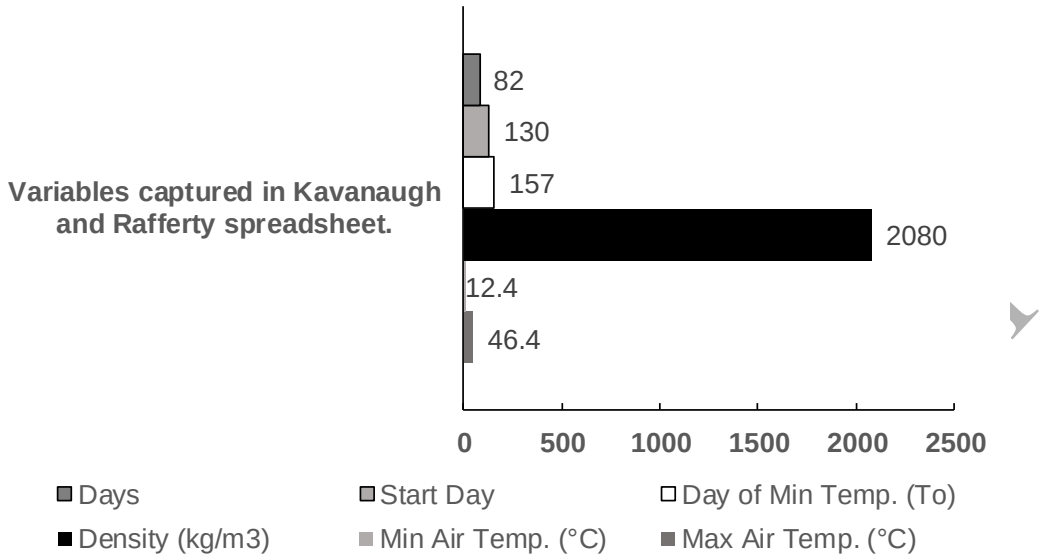

Figure 16. Variables captured in Kavanaugh and Rafferty spreadsheet of dry sand to a depth of 0.15 m.

Where *Max Air Temp* is the maximum average monthly air temperature; *Min Air Temp* is the minimum average monthly air temperature, °C; *Day of min temp* (To) is the number of days after January 1st when the minimum outdoor air temperature occurs, *Start Day* is the number of days after January 1st when cooling (or heating) season begins and *Days* is the number of days from the start of cooling (or heating) season until the day on which the analysis is made. Figure 17 shows a comparison between the results of the computational Kavanaugh and Rafferty model and the measured data.

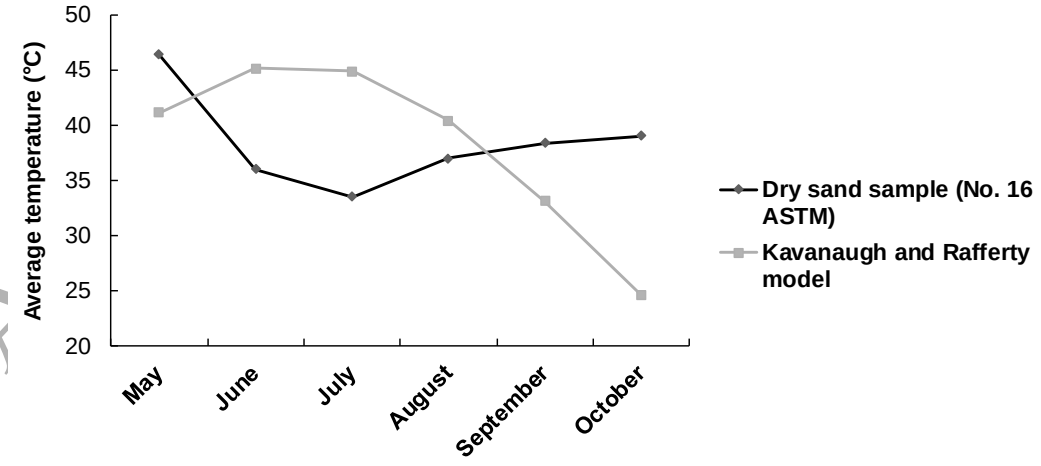

Figure 17. Comparison of the results from Kavanaugh and Rafferty spreadsheet and the temperatures of dry sand sample with No. 16 ASTM in 2017.

The results show that the average temperatures computed with the Kavanaugh and Rafferty model were different to the average measured temperatures in the sand sample with No. 16 ASTM from May to October, 2017. The Kavanaugh and Rafferty model, based on a spreadsheet, considers physical variables as thermal conductivity, specific heat and density of soil but it does not consider grain size and moisture of sandy soils. Figure 17 shows the necessity of updating the database of computational Kavanaugh and Rafferty model and include these two variables.

4.4 Mathematical models of soil temperature used in building simulation tools

Some commercial programs used by architects and engineers that design GHPS, consider equations to simulate the temperature profile of soil at different depths. For example, Energy Plus has the possibilkity to use two equations (DOE et al. 2016a). The first equation was developed by Kusuda and Achenbach (1965) to calculate the ground temperatures as function of depth and time. The second equation was developed by Xing (2014) to compute the average soil surface temperature in more than four thousand international locations. Simergy 2.4.2, which uses EnergyPlus as calculation engine, simulates the average soil temperatures with the first equation (DOE, DA, et al. 2016b). Nevertheless, most of commercial tools do not indicate in their manuals the equation used to compute the soil temperature nor do they consider the grain size of sand. Table 6 shows a list of programs which use mathematical models to simulate the soil temperature.

Table 6. Simulation programs for predicting the soil temperature.

Program	Authors of mathematical model
Energy Plus 8.6	Kusuda and Achenbach (Kusuda and Achenbach 1965) and Xing (Xing 2014)
Geo Designer 3.3.06	Not specified (ClimateMaster 2016)
GeoTSOL basic 2.0	Not specified (Valentin Software 2016)
GLD 2016	Not specified (Gaia 2016)
GroundTemp. and ResIP-SI14	Kavanaugh and Rafferty (Kavanaugh and Rafferty, 2014)
GLHEPro 5.0	Xing (Xing 2014)
Open Studio 1.12.0	National Renewable Energy Laboratory (NREL 2016), Kusuda and Achenbach (Kusuda and Achenbach 1965) and Xing (Xing 2014)
Simergy 2.4.2	Kusuda and Achenbach (Kusuda and Achenbach 1965) and Xing (2014)
Design builder 5.0.1.021	Kusuda and Achenbach (Kusuda and Achenbach 1965) and Xing (2014)
HyGCHP	Eskilson (Eskilson 1987)(Hackel 2016)
eQuest 3-65	Kavanaugh and Rafferty (Kavanaugh and Rafferty 1997)
Soil temperature	Nofziger; Hillel; Marshall; Holmes, and Wu (Nofziger et al. 2003)
ENVI-met V4	Michael Bruse (Bruse and Bruse 2017)

Figure 18 shows a simulation of sand temperatures with No. 16 ASTM (1.180 mm grain size) and the equation of Kusuda and Achenbach.This simulation used the following parameters: α= $9.80x10^{-7}$ m/s^2; day = Julian day (May 10th =130); day 0 = Phase constant = 0; A_s = $\left(\frac{T_{max.daily\ period} - T_{min.daily\ period}}{2}\right)$; T_m = 0.984 (T_{air}) +2.74; and T_{air} = air temperature at Netzahualcoyotl, Central Mexico (°C).

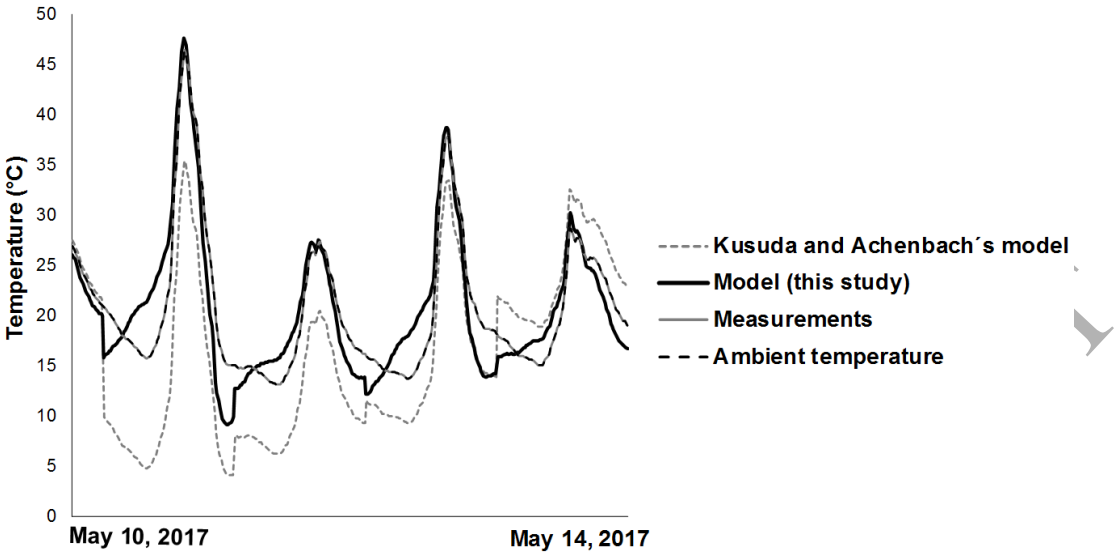

Figure 18. Temperatures computed with the Kusuda and Achebach´s model, the derived mathematical model and the measurements of temperature in the dry sand sample with No. 16 ASTM from May 10th to 14th, 2017.

Figure 19 shows a graph of the deviation between the measured temperatures in the beaker with dry sand with No. 16 ASTM and seven of the commercial programs. These programs calculated the temperature of dry sand at a depth of 0.15 m from May 16th to 31st, 2017.

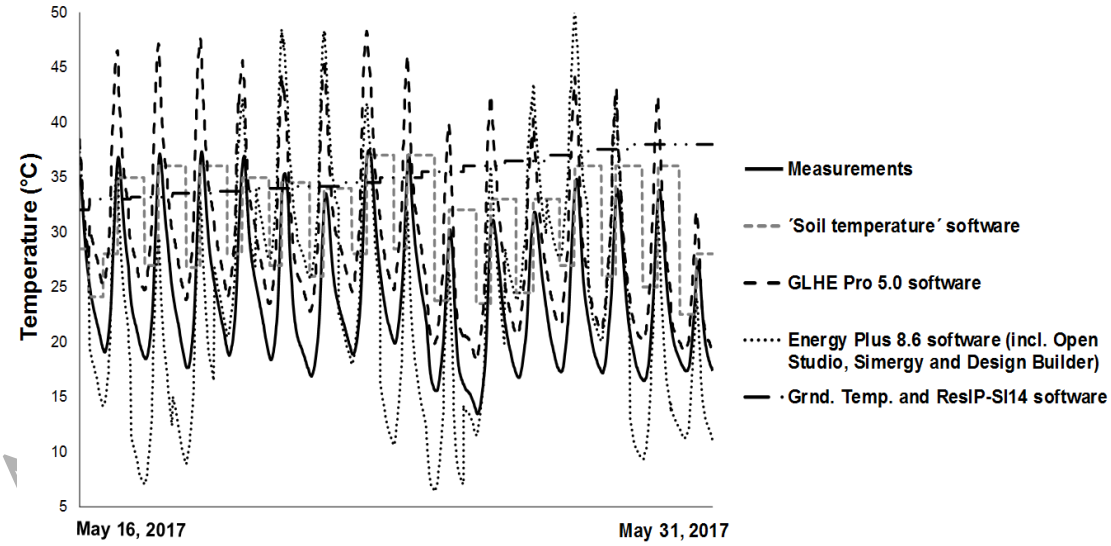

Figure 19. Deviation between the measured temperatures in the beaker with dry sand with No. 16 ASTM and seven of the commercial programs from May 16th to 31st, 2017.

In the case of the program '*Ground Temperature and ResIP-SI14'*, it could not simulate the measured temperatures of sand as is not able to compute time periods of 15 minutes or less. Additionally, the user cannot input values such as grain size and moisture into the section of ground properties. For the case of '*Open Studio', 'Simergy*' and '*Design Builder'*, they had similar thermal behaviour as all use EnergyPlus as simulation engine (using Kusuda-Achenbach and Xing equations). The calculated temperatures with these programs were close to temperatures of the sand sample.

The '*Soil temperature*' model provided a square shape temperature curve not close to the measured sand temperatures. The main reason is that the program only accepts few physical values for computing these temperatures and the user cannot input values for thermal conductivity, density, grain size and moisture of sand. Although, the program computed a fairly good approximation of maximum temperature, simulating 46 °C in the dry sand sample with No. 30 ASTM that had an actual temperature of 47.20 °C (Nofziger et al., 2003), the model failed to compute a good minimum temperature, as it provided 26.50 °C, where the actual minimum temperature was about 11.90 °C.

For '*GLHPro*' the simulated temperatures were higher due to the use of Xing´s equation. Xing´s equation uses the phase angle that it has not been calculated for our case study. Additionally, Xing´s equation considers the effects of weather conditions such as freezing/thawing of moisture in the soil but it does not consider the grain size. The author suggested that a value of the phase angle must be calculated for applications such as hourly energy analysis similar to the temperature measurements logged in this study (15 minutes).

4.5 Application of measured temperature data in a commercial program

To understand the potential application of the analysed sands as energy sources for GHPS, two commercial software have been used to simulate the performance of GHPS under the measured sand conditions: '*GeoTSOL'* and '*Geo Designer'*. These tools were selected as they can simulate the change in electricity consumption of GHPS as a function of soil type, temperature and sand moisture content. '*GeoTSOL'* has the capacity to consider soil type as input. The included soil types are wet, saturated, humid and dry sand and dolomite while the grain size can be defined as fine, coarse and sand rock. The names of sand types depend on percentage of water content of sand. On the other hand, '*Geo Designer'* can simulate sandy soils with similar thermal properties to the analysed

sands in this study. The assumed GHPS has a heating capacity of 17.57 kW and a variable speed fan. The temperatures of fluid close-loop sand heat exchanger ranged between 10°C - 40.56 °C. Table 7 and table 8 show the results from '*GeoTSOL'* and *'Geo Designer'* respectively.

Table 7. Results of annual simulation of different types of sand soils with GeoTSOL program (Valentin Software 2016).

Soil type	Heat pump electric consumption kWh/yr	Pumps electric consumption kWh/yr	Heating load (kW)	Geothermal Collector area (m^2)	Laying depth (m)	Ground water depth (m)	Spec. heat capacity (MJ/m^3K)	Ground water temp. (°C)	Conductivity (W/m K)	Water content (%)	Resulting heat extraction rate (W/m^2)
Wet sand	1,916	117	17.54	120	0.5	2.5	2.7	20	2.0	69	115
Saturated sand	2,000	124	17.54	120	0.5	2.5	2.7	10	2.4	60	115
Humid sand	2,091	132	17.54	120	0.5	2.5	1.9	10	1.4	40	115
Dry sand	2,274	147	17.54	120	0.5	2.5	1.5	10	0.4	20	115
Sand stone	1,989	123	17.54	120	0.5	2.5	2.3	10	2.8	10	115
Dolomite brick	1,972	122	17.54	120	0.5	2.5	2.3	10	3.5	10	115

Table 8. Results of simulation of different types of sand soils with Geo Designer program (ClimateMaster 2016).

Soil type	Heat pump electric consumption (kWh)	Average COP	Heating load (kW)	Pipe type (Dia. 2.54 cm)	Pipe Configuration	Avg. Pipe Depth (m)	Bore Length (m)	Deep Earth Temperature (°C)	Heating Run Time (h)	Soil Conductivity (W/mK)
Dry sand/ Gravel	2,073	4.75	14.62	IPS HDPE SDR 11	U-Tube Horizont. Bore	7.62	591.46	17.78	627	0.61
Damp sand/ Gravel	2,073	4.76	14.62	IPS HDPE SDR 11	U-Tube Horizont. Bore	7.62	239.33	17.78	625	1.56
Saturated sand/ Gravel	2,073	4.77	14.62	IPS HDPE SDR 11	U-Tube Horizont. Bore	7.62	163.11	17.78	624	2.49
Avg. Rock	2,073	4.77	14.62	IPS HDPE SDR 11	U-Tube Horizont. Bore	7.62	169.21	17.78	623	2.42

Table 7 shows the relationship between the water content percentage of sands and electricity consumption in the heating mode of the heat pump. The water content percentage decreased from 69 % to 10 % while the electricity consumption increased from 1,916 kWh/yr to 2,274 kWh/yr. This table also illustrates that the change of soil of dry sand to sand stone decreases the electricity consumption of the heat pump from 2,274 kWh/yr to 1,989 kWh/yr.

Table 8 shows a decrease of bore length between dry and saturated sand. The bore length decreased from 591.46 m to 163.11 m with the increase of moisture. These outputs also show a decrease of bore length between dry sand and average rock (591.46 m-169.21 m). This decrease is caused by different factors such as the change of grain size and soil thermal conductivity. The decrease of bore length causes a decrease of power and electricity consumption of centrifugal pump because less amount of water must flow in horizontal U-Tube of the GHPS. The measured temperatures in the wet sands with No. 50, 30, and 16 ASTM could be used to update the database of programs such as the ones used in this study.

5. Conclusions

In this study, experiments on different sand samples under different conditions were conducted aimed at developing a novel mathematical model to predict thermal behaviour of sand considering different physical variables.

From the observations, it can be deducted that when sand is exposed to solar radiation, grain size has a direct influence on the sand temperature where fine-grained sand attains a higher maximum temperature than coarse-grained sand. However, the thermal behaviour also depends on factors such as grain shape, grain size, grain color, and moisture content. Sub-angular and rounded grains absorbed heat better than angular or sub-rounded shape grains as the former have more surface area in contact, where the sub-angular grains can function as fins do in a heat exchanger. Quartz grains with sub-angular shape increase physical contact points between dry sand grains and the heat flux paths.

Experimental data showed that sand of sub-angular and rounded grain shapes, small grain size (No. 50 ASTM and No. 30 ASTM), and moisture content between 0 % and 24.9 %

enclosed within a metal container covered with glass, could have the capacity to increase performance efficiency of a GHPS in heating mode. The smaller the temperature difference required for indoor air conditioning, the lower the work done by the GHPS compressor.

Although some simulation programs have the capability to simulate the temperature of sandy soils, these programs use mathematical correlations that are not able to adequate simulate the thermal behaviour of sand in specific regions as they do not account parameters such as the size and grain shape. The derived mathematical model provided more accurate approximations compared to the actual temperatures in dry regions. This model could be implemented in building simulation tools that aim to increasing the calculation accuracy, optimize equipment size and borehole length. The minimisation of borehole length would reduce power and electricity demand of centrifugal pumps, thus decreasing the electricity bill of the GHPS.

For future work, it is intended to include the derived model into a building simulation tool such as EnergyPlus or TRNSYS. In this way, it would be possible to perform dynamic simulations with the aim to gain at deeper understanding of the year-round technical performance of a GHPS in this type of sand soils.

Nomenclature

Symbol	Name	Unit
A_s	*Annual temperature amplitude of soil surface*	°C
$A(z)$	*Amplitude at depth z*	°C
A_0	*Annual temperature amplitude on soil surface*	°C
A_{0y}	*Vertical component of annual temperature amplitude*	°C
C	*Geothermal gradient on surface of soil*	°C/m
d_G	*Grain size*	mm, μm
d^2T	*Second differential temperature*	°C
$\frac{dT}{dt}$	*Differential temperature divided into differential time*	°C/m
dz^2	*Second differential depth*	m
D	*Damping depth*	m
F	*Range damping factor is 0.45 for intermediary climate in sandy soil*	-
G	*Heat flux by time and volume*	W/m^3

k_{soil}	*Soil thermal conductivity*	W/m K
k_s	*Sand thermal conductivity*	W/m °C
L	*Time lag per meter depth*	Day/m
m_{soil}	*Soil mass*	kg
m_s	*Sand mass*	kg
MAD	*Median Absolute Deviation*	-
n	*Amount of grains*	-
N	*Number of temperature measurements of period*	-
SH_{soil}	*Soil specific heat*	J/kg K
SH_s	*Soil specific heat*	J/kg °C
t	*Time of measure of soil temperature*	s
t_e	*Boundary condition of time*	s
Δt	*Time variation*	s
T	*Temperature on soil surface*	°C
T_{DMM}	*Temperature of sand sample that was computed to the derived mathematical model*	°C
T_m	*Mean temperature on soil surface*	°C
T_s	*Soil temperature on day t at depth z*	°C
T_{ss}	*Sand surface temperature*	°C
T_{sos}	*Soil surface temperature*	°C
T_0	*Soil surface temperature in site*	°C
T_o	*Number of days after January 1 when minimum outdoor air temperature occurs*	°C
V_s	*Sand volume*	m^3
x	*Volume fraction of each component of soil*	-
z_1	*Depth of 0*	m
z	*Soil and sand depth*	m

Greek symbols

Symbols	Name	Unit
α	*Thermal diffusivity of soil*	m^2/s
α_{soil}	*Thermal diffusivity od soil*	m^2/s
φ	*Second angular displacement*	rad

ρ_g	*Density of gaseous component of soil*	kg/m^3
ρ_l	*Density of liquid component of soil*	kg/m^3
ρ_s	*Density of sand*	kg/m^3
ρ_{so}	*Density of solid component of soil*	kg/m^3
ρ_{soil}	*Soil density*	kg/m^3
ω	*Angular speed in a simple harmonic motion*	rad/s

Acknowledgments

The authors would like to thank the Preparatory National School, UNAM for facilities granted for the use of its computer center and microscope.

This research did not receive any specific grant from funding agencies in the public, commercial, or not-for-profit sectors.

References

Abu-Hamdeh, N. H., A. I. Khdair, and R.C. Reeeder. 2001. A comparison of two methods used to evaluate thermal conductivity for some soils. International Journal of Heat and Mass Transfer 44(5):1073-1078.

Anderson, D. R., Sweeney, D. J., and T. A. Williams. 1999. Statistics for Business and Economy. Predictions (7th. pp. 766-767). New York: South Western College Publishing.

ASTM, 2013. D4365-13 Standard Test Method for Determining Micropore Volume and Zeolite Area of a Catalyst. ASTM International, West Conshohocken, PA. https://doi.org/10.1520/D4365-13

Baruch, G. 1994. The earth as a cooling source for buildings. In J. Wiley (Ed.), Passive low energy cooling of buildings (1 st., pp. 1–272). New York: John Wiley and Sons, Inc.

Beier, R. A., M. D. Smith, and J. D. Spitler. 2011. Reference data sets for vertical borehole ground heat exchanger models and thermal response test analysis. Geothermics, 40(1):79–85.

Bleicher, A., and M. Gross. 2016. Geothermal heat pumps and the vagaries of subterranean geology: Energy independence at a household level as a real world experiment. Renewable and Sustainable Energy Reviews 64: 279–288.

Bruse, M., and D. Bruse. 2017. ENVI-MET. Essen: ENVI_MET GmbH.

Campbell, G. S., and J. M. Norman. 1998. Heat Flow in the Soil. In Springer-Verlag (Ed.), An Introduction to Environmental Biophysics (2nd ed., pp. 113–128). New York: Springer.

Cengel, Y. 2004. Table A-8. Properties of Miscellaneous Materials. McGraw-Hill/Interamericana Editores, S.A de C.V. (Ed.), Heat Transfer, A Practical Approach (2nd ed., p. 729). Mexico City: Mc Graw Hill Interamericana.

Chen, S. X.2008. Thermal conductivity of sands. Heat and Mass Transfer 44:1241-1246.

ClimateMaster. 2016. GeoDesigner. Oklahoma: ClimateMaster.

Del Rio-Moreno, H. (2019, January 8th). Chief Laboratoris, Mexican Institute of Petroleum (IMP). Interview.

Derradji, M., and M. Aiche. 2014. Modeling the soil surface temperature for natural cooling of buildings in hot climates. Procedia Computer Science 32: 615–621.

DOE, BTO, and NREL. 2016. Energy Plus. Denver, CO: U.S. Department of Energy, Building Technologies Office and National Renewable Energy Laboratory.

DOE, DA, LBNL, TRANE, NEEA, HYDRO QUEBEC, and INFOSYS. 2016. Simergy. Washington D.C.: Digital Alchemy.

Eskilson, P. 1987. Thermal analysis of heat extraction boreholes. Lund University.

Gaia. 2016. Ground Loop Design. Maple Plain, Minnesota: Thermal Dynamics Inc.

Garcia-Padron, R., Loyd, D., Sjökvist, S., 2002. Heat and Moisture Transfer in Wet Sand Exposed to Solar Radiation—Models and Experiments Concerning Buried Objects. Subsurface Sensing Technologies and Applications 3(2): 125-150.

Hackel, S. 2016. HyGCHP modeling tool. Madison, Wisconsin: Seventhwave.

Hakkaki-Fard, A., Eslami-Nejad, P., Aidoun, Z., Ouzzane, M. 2015. A techno-economic comparison of a direct expansion ground-source and an air-source heat pump system in Canadian cold climates. Energy 87: 49-59.

Herb, W.R., Janke, B., Mohseni, O., and H. G. Stefan. 2008. Ground surface temperature simulation for different land covers. Journal of Hydrology 356: 327-343.

Hepbasli, A., Akdemir, O., and E. Hancioglu. 2003. Experimental study of a closed loop vertical ground source heat pump system. Energy Conversion and Management 44: 527–548.

Jebalamar, A. S., Thambi, S. A., and S. J. Sunhita. 2012. Prediction of annual and seasonal soil temperature variation using artificial neural network. Indian Journal of Radio and Space Physics 41: 48-57.

Jin, H., Wang, Y., Zheng, Q., Liu, H., and E. Chadwick. 2017. Experimental study and modelling of the thermal conductivity of sandy soils of different porosities and water contents. Applied Sciences 7(2), 119: 1-17.

Jutglar, L., A. L. Miranda, and M. Villarrubia. 2011. Respeto al medio ambiente, Geotermia. In J. Boixareu (Ed.), Manual de calefacción (1a., pp. 517–546). Barcelona: Marcombo.

Kavanaugh, S. P., and K. Rafferty. 2014. Geothermal Heating and Cooling, Design of Ground-Source Heat Pump Systems. Atlanta: ASHRAE.

Kavanaugh, S. P., and K. Rafferty. 1997. Ground Source Heat Pumps: Design of Geothermal Systems for Commercial and Institutional Buildings. ASHRAE, 1–167.

Kupiec, K., Larwa, B., and M. Gwadera. 2015. Heat transfer in horizontal ground heat exchangers. Applied Thermal Engineering 75: 270-276.

Kusuda, T., and P. R. Achenbach. 1965. Earth Temperatures and Thermal Diffusivity at Selected Stations in the United States. Washington, D.C.

Luo, J., Z. Luo, J. Xie, D. Xia, W. Huang, H. Shao, W. Xiang, and J. Rohn. 2018. Investigation of shallow geothermal potentials for different types of ground source heat pump systems (GSHP) of Wuhan city in China. Renewable energy 118: 230-244.

Luo, J., J. Rohn, W. Xiang, D. Bertermann, and P. Blum. 2016. A review of ground investigations for ground source heat pump (GSHP) systems. Energy and Buildings 117: 160-175.

Meline, L. and S. Kavanaugh. 2017. Grounded In Reality: Better Ground Source Heat Pump Design. Geo Outlook. 36–40. http://geooutlook.org/epub/GO2017No2/.

Monteith, J. L., and M. H. Unsworth. 2013. Steady-State Heat Balance. In A. Press (Ed.), Principles of Environmental Physics Plants, Animals and the Atmosphere (4th ed., pp. 217–247). San Diego: ELSELVIER.

Nobel, P. S., and G. N. Geller. 1987. Temperature modeling of wet and dry desert soils. Journal of Ecology, 75(1): 247–258.

Nofziger; Hillel; Marshall; Holmes, and Wu. 2003. Soil temperature. Stillwater: Oklahoma State University.

Noorollahi, Y., Saeidi, R., Mohammadi, M., Amiri, A., and M. Hosseinzadeh. 2018. The effects of ground heat exchanger parameters changes on geotermal heat pump performance – A review. Applied Thermal Engineering 129: 1645–1658.

NREL. 2016. Open Studio. Denver, CO: National Renewable Energy Laboratory and the Alliance for Sustainable Energy, LLC.

Ozgener, O., Ozgener, L., and W. J. Tester. 2013. A practical approach to predict soil temperature variations for geothermal (ground) heat exchangers applications. International Journal of Heat and Mass Transfer 62: 473-480.

Poudel, B., Poudel, P. C., and S. Gurung. 2012. The modeling of soil temperature with depth. Tribhuvan University: 1-8.

Shang, Y., Dong, M., and S. Li. 2014. Intermittent experimental study of a vertical ground source heat pump system. Applied Energy 136: 628–635.

Spilker EH. 1998. Ground-coupled heat pump loop design using thermal conductivity testing and the effect of different backfill materials on vertical bore length. ASHRAE Transactions; 104(1B):775–779.

US Department of Agriculture, D. of E. and E. P. 2016. Evaluation Criteria. Soil Suitability for Closed-Loop Horizontal Residential Geothermal Heat Pumps, State of Connecticut. Norwich.

Valentin Software. 2016. GeoTSOL basic. Berlin: Valentin Software, Inc.

Wang, Z., Zhang, N., Lin, F., Ding, J., and H. Yang. 2019. Thermal conductivity of dry sands treated with Microbial –Induced Calcium Carbonate Precipitation. Advances in Materials Science and Engineering: 1-8.

Wood, C. J., Liu, H., and S.B. Riffat. 2010. An investigation of the heat pump performance and ground temperature of a piled foundation heat exchanger system for a residential building. Energy 35: 4932–4940.

Xing, L. U. 2014. Estimations of undisturbed ground temperatures using numerical and analytical modeling. Oklahoma State University.

Yang, W., Kong, L., and Y. Chen. 2015. Numerical evaluation on the effects of soil freezing on underground temperature variations of soil around ground heat exchangers. Applied Thermal Engineering 75: 259–269.

Yener, D., Ozgener, O., and Ozgener, L. 2017. Prediction of soil temperatures for shallow geothermal applications in Turkey. Renewable and Sustainable Energy Reviews 70: 71-77.

You, T., W. Wu, W. Shi, B. Wang, and X. Li. 2016. An overview of the problems and solutions of soil thermal imbalance of ground-coupled heat pumps in cold regions. Applied Energy 177: 515–536.

You, T., X. Li, W. Wu, W. Shi, B. Wang, and K. Soga. 2017. Coupled heating of ground-coupled heat pump system with heat compensation unit: Performance improvement and borehole reduction. Energy Conversion and Management 148: 57–67.

Zhang, N., Yu, X., Pradhan, and A. J. Puppala. 2015a.Thermal conductivity of quartz sands by thermo-TDR probe and model prediction. ASCE Journal of Materials in Civil Engineering 27(12).

Zhang, N., Yu, X., Pradhan, A., and A. J. Puppala. 2015b. Effects of particle size and fines content on thermal conductivity of quartz sands. Transportation Research Record: Journal of the Transportation Research Board 2510: 36-43.

Zhang, N. and Z. Wang. 2017. Review of soil thermal conductivity and predictive models. International Journal of Thermal Sciences 117: 172-183.